

Fracture behaviour of a Fe–22Mn–0.6C–0.2V austenitic TWIP steel

Julie Lorthios, Matthieu Mazière, Xavier Lemoine, Philippe Cugy, Jacques Besson, Anne-Françoise Gourgues-Lorenzon

▶ **To cite this version:**

Julie Lorthios, Matthieu Mazière, Xavier Lemoine, Philippe Cugy, Jacques Besson, et al.. Fracture behaviour of a Fe–22Mn–0.6C–0.2V austenitic TWIP steel. International Journal of Mechanical Sciences, 2015, 101-102, pp.99-113. 10.1016/j.ijmecsci.2015.07.029 . hal-01199574

HAL Id: hal-01199574

https://minesparis-psl.hal.science/hal-01199574

Submitted on 15 Sep 2015

HAL is a multi-disciplinary open access archive for the deposit and dissemination of scientific research documents, whether they are published or not. The documents may come from teaching and research institutions in France or abroad, or from public or private research centers.

L'archive ouverte pluridisciplinaire **HAL**, est destinée au dépôt et à la diffusion de documents scientifiques de niveau recherche, publiés ou non, émanant des établissements d'enseignement et de recherche français ou étrangers, des laboratoires publics ou privés.

Fracture behaviour of a Fe-22Mn-0.6C-0.2V austenitic TWIP steel

Julie Lorthios[1,a], Matthieu Mazière[1], Xavier Lemoine[2], Philippe Cugy[2,b], Jacques Besson[1], Anne-Françoise Gourgues-Lorenzon[1]*

[1]MINES ParisTech, PSL Research University, Centre des Matériaux, UMR CNRS 7633, BP87, 91003 Evry cedex, France
[2]ArcelorMittal Maizières Research and Development, R&D Automotive Products, BP 30320, 57283 Maizières-lès-Metz cedex, France

[a]Now at EDF – CEIDRE - DETU, 2 rue Ampère, 93206 Saint-Denis Cedex 01 email : julie.lorthios@edf.fr
[b]Now at Aperam Alloys Imphy, BP 1, 58160 Imphy, France
*Corresponding author. Phone: (+33) 1 60 76 30 66 Fax: (+33) 1 60 76 31 50
email: anne-francoise.gourgues@mines-paristech.fr

Abstract

The mechanical behaviour of a 22Mn-0.6C-0.2V austenitic TWIP steel has been extensively characterised for a variety of strain ratios (from shear to biaxial stretching) using smooth and notched specimens. A constitutive model involving a non-isotropic yield function together with isotropic and/or kinematic hardening satisfactorily represented the experimental database. It was used to estimate local stress and strain fields and to derive a fracture criterion based on the equivalent stress and Lode angle that were expressed to be consistent with the constitutive equations describing the plastic flow behaviour. A weak dependence on hydrostatic stress further improves prediction of fracture initiation, with an average standard error of less than 5% over ten different mechanical tests.

Keywords

Plastic yield anisotropy; ductile fracture; anisotropic fracture criterion; TWIP steels; forming limit diagram

1. Introduction

Among Advanced High Strength Steels (AHSSs), high carbon, high manganese austenitic twinning-induced plasticity (TWIP) steels offer an excellent compromise between strength and formability (see e.g. [Cornette et al, 2005]) particularly suitable to lightweight automotive applications. Relationships between their microstructure and mechanical properties have been recently reviewed [Bouaziz et al, 2011]. The high work-hardening of these steels relies on complex interactions between solid solution carbon atoms, dislocation glide and intense mechanical twinning, owing to their low stacking fault energy close to room temperature.

The high carbon content of these steels induces thermal activation of dislocation glide (contribution of ~70 MPa to effective stress close to room temperature for a Fe-22Mn-0.6C steel [Bouaziz et al, 2011]) and pronounced dynamic strain ageing (DSA) attributed to complex interactions between carbon atoms and dislocations [Lee et al, 2011]. Serrated yielding and negative strain rate sensitivity have commonly been reported under uniaxial tension under low strain rates [e.g. Bayraktar et al, 2004, Scavino et al, 2010]. The high strain hardening stems from mechanical twins acting as obstacles to dislocation glide [see e.g. Rémy, 1978, Idrissi et al, 2010]).These steels also exhibit a strong anisotropy in plastic yielding, in spite of weak initial texture in the cold rolled + annealed state [Gutierrez-Urrutia et al, 2010, Barbier et al, 2009]. Constitutive modelling of TWIP steels made use of either Hill's anisotropic criterion [e.g. Chung et al, 2011] or anisotropic criteria developed by Barlat et al. [Chung et al, 2011, Xu et al, 2012] and satisfactorily reproduces the uniaxial tensile and hole expansion behaviour of these materials by proper fitting of model parameters [Chung et al, 2011, Xu et al, 2012].

In spite of their high formability, high manganese TWIP steels are sensitive to abrupt slant fracture under a variety of loading modes. This uncommon behaviour makes diffuse necking criteria [Dorn and Thomsen 1947, Swift 1952] as well as localised necking criteria [Hill, 1952, Marciniak and Kuczynski, 1967] not suitable to describe the formability of this material [Chung et al, 2011]. Intense deformation bands that develop under uniaxial tension have been reported to assist initiation of abrupt fracture [De Cooman et al, 2008, Scavino et al, 2010, Wang et al, 2011]. Under biaxial stretching [Scavino et al, 2010] as well as stamping of real parts [Allain et al, 2008], no localisation band could be experimentally detected whereas the sensitivity to loading rate is negative and slant fracture still may occur without any noticeable reduction in thickness. Fracture surfaces exhibit two populations of dimples. Coarser dimples, often elongated along the rolling direction (RD), have been reported [Xu et al, 2012, Lorthios et al, 2010]. They have been attributed to either decohesion of MnS stringers from the matrix [Xu et al, 2012] or to the coalescence of groups of smaller voids, whose anisotropic shape was consistent with anisotropy in plastic strain [Lorthios et al, 2010]. The volume fraction of such voids is yet very low (typically below 0.2% even close to the fracture surface) and the vast majority of the fracture surface at room temperature exhibits submicrometer-sized dimples. Their nucleation and coalescence mechanisms, although attributed to the coalescence of nano-voids by [Abbasi et al, 2009], are still unclear [e.g. Bouaziz et al, 2011]. Except for the very low quantity of coarser voids, no sign of damage has been evidenced by metallographic observation of fractured specimens.

Phenomenological fracture criteria have been developed to tentatively predict the forming limit diagram of TWIP steels [e.g. Chung et al, 2011b]. They make use of one, or several of the following parameters: the maximum shear stress, τ_{max} (Tresca-type criterion) [Bouaziz et al, 2011], the stress triaxiality, the equivalent stress and the Lode parameter, which is a function of the second and third invariants of the deviatoric stress tensor that enables e.g. axisymmetric stress states to be conveniently distinguished from plane strain. While the plastic strain anisotropy of high-manganese TWIP steels has been extensively studied [Xu et al, 2012, Barbier et al, 2009], their anisotropy in fracture has only been scarcely addressed [Lorthios et al, 2010, Xu et al, 2012]. In the above mentioned fracture criteria, invariants of stress tensors have generally been derived using a von Mises-based formalism, whatever the formalism of constitutive equations. On the other hand, a fracture criterion expressed with the same formalism as that of constitutive equations has already been used (with a Hill-type yield criterion) by [Beese et al, 2010] to predict slant fracture of an aluminium alloy but, to the authors' knowledge, such an approach has never been reported for TWIP steels.

The objective of this study is to characterise both yield and fracture anisotropy of a Fe-22Mn-0.6C-0.2V TWIP steel, to derive a failure criterion that could be applied for the determination of forming conditions. The fracture criterion makes use of the *same* formalism as that used in constitutive equations to provide a homogeneous framework for the mechanical analysis of forming tests. In addition, this study aims at getting more insight into the physical fracture mechanisms, including the effect of mechanical twinning and stress state.

2. Materials and experimental procedures

2.1. Material

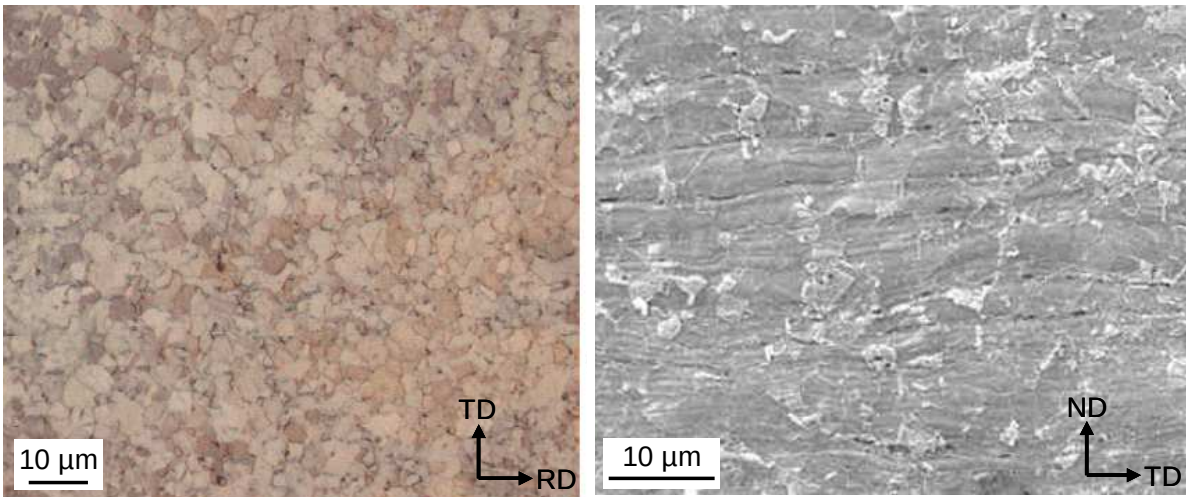
A Fe-22Mn-0.6C austenitic TWIP steel was provided as a bare 1.5-mm-thick cold-rolled and annealed sheet. Its chemical composition is reported in Table 1. The average grain size is about 3 µm (Fig. 1a), with some segregation bands visible throughout the sheet thickness (Fig. 1b). Due to the low thickness of these bands, no electron probe microanalysis was conducted to determine their chemistry but they are supposed to stem from manganese segregation. They did not interact with the appearance of fracture surfaces, so that they are no longer considered in the following of this paper. The average chemical composition yields a low value of the stacking fault energy (about 20 $mJ.m^{-2}$ at room temperature) together with thermally-activated dislocation glide, so that this material may deform with intense mechanical twinning without any detectable austenite-to-martensite phase transformation [e.g.

Scott et al, 2005, Allain et al, 2004] in agreement with Schumann's diagram [Schumann, 1972]. Vanadium carbides are known to increase the yield strength by interacting with dissociated partial dislocations [Yen et al, 2012]. A resulting contribution to the effective stress of around 140 MPa has been reported for a steel of similar chemical composition and grain size [Scott et al, 2011]. Carbides also decrease the sensitivity of the steel to delayed hydrogen-assisted cracking [Malard et al, 2012].

Table 1: Chemical composition of the investigated TWIP steel (wt%)

Fe	Mn	C	V	S
base	22	0.6	0.2	0.0008

In the following, RD, TD, ND and DD respectively denote the rolling direction, transverse direction, sheet normal and diagonal direction (i.e. at 45° from RD in the (RD, TD) plane). All investigations were carried out in laboratory air, at room temperature with full-thickness specimens, unless otherwise stated.



(a) (b)

Figure 1: Microstructure of the Fe-22Mn-0.6C-0.2V TWIP steel. (a) Grain morphology (light optical micrograph, electrolytic etch with a Struers® A2 solution), (b) segregation bands (scanning electron micrograph, secondary electron imaging, colloidal silica finish).

2.2. Uniaxial tensile tests

Uniaxial tensile (UT) dogbone specimens (60 x 12.5 mm^2 in gauge) were cut along RD, TD and DD and pulled in tension with an elongation rate of 4.10^{-4}, 4.10^{-3} and 4.10^{-2} s^{-1} in a 250 kN MTS servohydraulic machine equipped with a 50 kN load cell. Two specimens were used per testing condition. Axial elongation was recorded using a 9-mm-gauge extensometer. The reduction in width was monitored using a clip extensometer attached to the central part of the gauge region. The Lankford coefficient, r_d (d being the loading direction), was calculated as the ratio between logarithmic plastic strain along the specimen width to that along ND. To this aim, an isochoric assumption was made, consistently with reported very low level of porosity even at fracture [Lorthios et al., 2010].

High strain rate uniaxial tension tests were carried out along RD using an Instron high-speed machine, with a specific dogbone specimen having a 65 x 9 mm^2 or a 65 x 11 mm^2 gauge part. One specimen was used per testing condition and geometry. Both geometries yielded similar results. The load was calculated from elastic deformation of strain gauges fixed to one end of the specimen. A laser extensometer was used for axial strain measurements. For the two selected elongation rates (50 s^{-1} and 110 s^{-1}), self-heating of the specimen did not exceed 100°C during the test, which should not change the deformation mechanism of this material.

To investigate the possible influence of mechanical twinning on the fracture mechanism, additional UT tests were carried out at 400°C along RD and TD with a 100 kN MTS servohydraulic machine fitted with a radiation furnace. The temperature was monitored using a K-type thermocouple spot-welded onto the centre of the gauge part. Two other thermocouples were spot-welded at either end of the gauge part. A smaller specimen geometry (30 x 4 mm^2 in gauge) was selected and a muffle was placed around the specimen to reduce the temperature gradient to less than ±10°C. The average axial strain was continuously monitored using an extensometer attached to the gauge part (gauge length 10 mm). As deformation under UT loading may be very heterogeneous in Hadfield steels [Dastur and Leslie, 1981, Owen and Grujicic, 1998, Canadinc et al, 2008, Renard et al, 2010] and TWIP steels [Alain, 2004, Chen et al, 2007, Lebedkina et al, 2009, Zavattieri et al, 2009], the effect of specimen geometry was tested at room temperature, along RD (one specimen), with an elongation rate of 4.10^{-2} s^{-1} by comparison with the above mentioned UT tests on larger specimens. Tensile curves were superimposed with reproducibility better than 3%. At 400°C, the strain rate sensitivity was evaluated along RD with elongation rates of 10^{-5}, 4.10^{-5}, 8.10^{-5}, 4.10^{-4} and 4.10^{-2} s^{-1}. Two specimens were used for each condition and yielded very reproducible results, both for tensile curves and fracture modes.

2.3. Reverse shear tests

The Bauschinger effect was evaluated by reverse shear tests carried out with a 45 x 30 mm^2 specimen geometry and a loading rate of 500 $N.s^{-1}$. The shear direction was parallel to TD and displacement along RD was precluded. Fiducial marks together with a camera were used to derive the engineering shear strain, e_{12}. The engineering shear stress, σ_{12}, was calculated as the applied load (i.e. along TD) divided by the specimen width and thickness. Monotonic tests were carried out up to fracture, which occurred close to the grips. As a consequence, these tests could not be used to assess damage and fracture under shear loading. The Bauschinger effect was determined by loading the specimen up to a maximum value, e_{max}, of e_{12} (0.025, 0.05, 0.10, 0.15 or 0.20), then unloading and applying immediately the load along the reverse direction until e_{12} reached at least -0.1.

2.4. Tensile tests on notched specimens

Double edge, U-notched tensile specimens with a minimum width of 10 mm, a notch depth of 2 mm and a notch radius of 2 mm (DENT2), 1 mm (DENT1) or 0.5 mm (DENT05) were pulled in tension using the same set-up as for room temperature UT tests at low strain rates. For every notch radius, two specimens were tested along each of the RD, TD, and DD directions, with prescribed load line displacement rate of 0.5 $mm.min^{-1}$. The notch opening (recorded using clip extensometers) vs. time curves (one for either notch) did not differ by more than 3.4%, so that only values of notch opening averaged over both notches are reported here for a given specimen. The effective stress (i.e. load divided by initial value of the area between notches) was plotted as a function of notch opening. For some additional specimens (one DENT2 and one DENT05 for both RD and TD directions), a digital image correlation system was used to monitor strain fields. It consisted of a 2448 x 2050 $pixel^2$ camera fitted with the Aramis™ software [GOM]. A random speckle was deposited on one side by use of acrylic painting. 0.35 x 0.35 mm^2 regions were used for image correlation, with a recording rate of 0.2 up to 1 frame per second. Logarithmic strain fields were derived from displacement field calculations, with a spatial resolution of 0.2 to 0.4 mm depending on specimen geometry.

To investigate a variety of loading modes by still using a UT testing facility, more complex specimens were also selected. An in-plane double edge notched shear (DENS) specimen was designed after that used by [Brünig et al, 2008] for aluminium alloys, both with or without spherical-cap-shaped side grooves (specimen geometry illustrated below together with the results).The aim of these tests was to characterise the fracture behaviour at near-zero hydrostatic stress. Specimens were cut along RD and TD and pulled in tension with an electrical-mechanical Zwick testing machine, with prescribed load line displacement of 0.17 $mm.s^{-1}$. In contrast to [Brünig et al, 2008], specimen ends were clamped in grips to avoid premature failure that could occur at high loads around holes. Some slipping was sometimes observed, so that the strain field monitoring technique was systematically used in the same conditions as previously mentioned.

Double side notched tensile (DSNT) specimens were used to localise strain within a band tilted by 45° with respect to the sheet plane and loading direction, to reproduce the geometry of slant fracture [McClintock & Argon, 1966]. The notches were perpendicular to the loading direction, but not in front of each other. The digital image correlation technique was used to monitor strain field at one edge of the specimen. Two specimens were tested along each of the RD and TD directions, with prescribed load line displacement rate of 0.1 mm.s^{-1}.

To tentatively interrupt crack propagation and study damage development ahead of the crack tip, single edge notched Kahn-type specimens [ASTM 1996] were pulled in tension parallel to RD, the crack propagating along TD (RD-TD orientation) or vice versa (TD-RD orientation). Owing to the high forming ability of the steel, extensive buckling occurred and hindered mechanical analysis of these tests. However, crack propagation could be arrested to investigate damage development by metallographic techniques.

2.5. Metallographic observation of tested specimens

All fracture surfaces were examined by scanning electron microscopy (SEM), in the secondary electron imaging mode, using either a Leo 1450VP or a Shottky-field emission gun Zeiss DSM 982 Gemini microscope fitted with X-ray energy dispersive spectrometry (EDX). Kahn-type specimens containing arrested cracks were observed in cross-section after conventional polishing followed by a colloidal silica finish. Microtomographic observations close to one of these cracks have already been reported elsewhere [Lorthios et al, 2010].

3. Experimental results and discussion

3.1. Uniaxial tensile behaviour

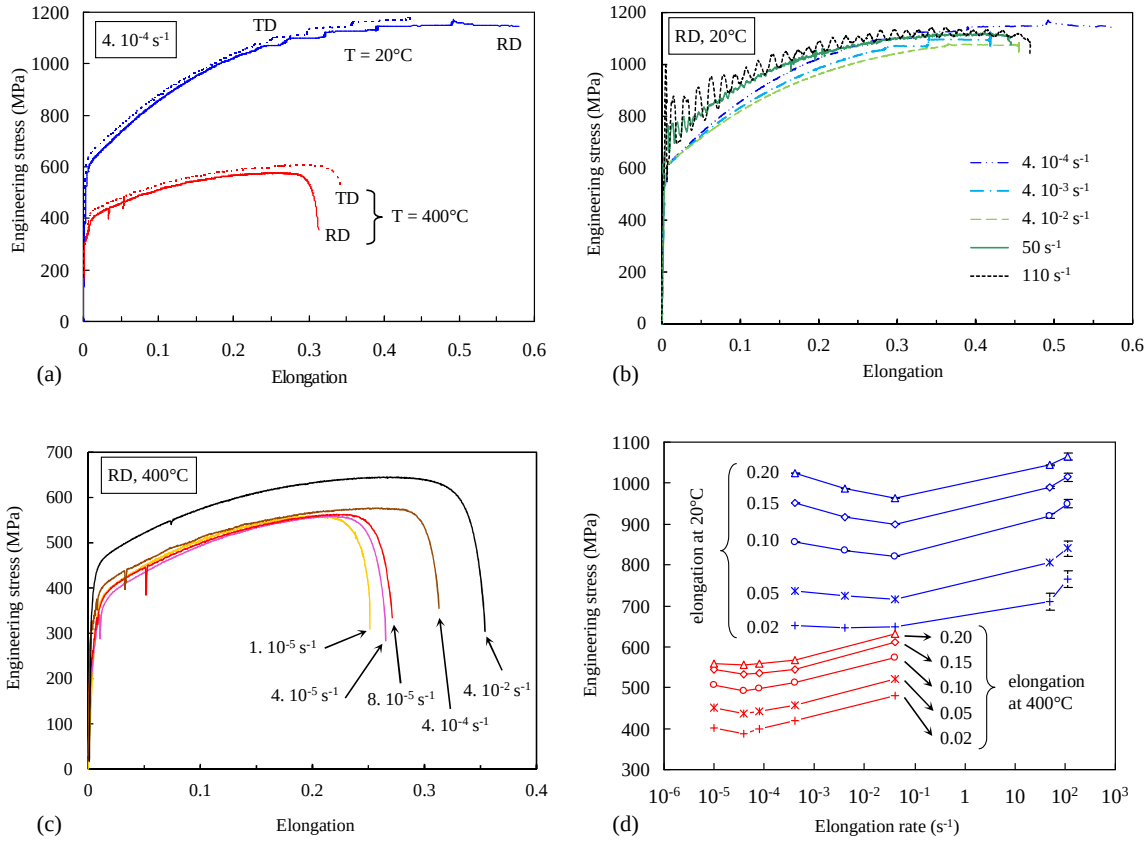


Figure 2: Engineering stress-strain curves under uniaxial tension. (a) Effect of the loading direction; strain rate sensitivity (b) at room temperature, (c) at 400°C, and (d) at both (loading along RD).

Table 2: Room temperature uniaxial tensile properties of the Fe-22Mn-0.6C-0.2V material. Values of strength for higher elongation rates are only indicative due to load oscillations (propagation of elastic waves)

Loading direction	Elongation rate (s^{-1})	Yield strength (MPa)	Tensile strength (MPa)	Fracture elongation (%)	Lankford coefficient, *r*	Logarithmic reduction of thickness at fracture
RD	4.10^{-4}	442	1137	35; 58	0.87	0.37; 0.41
	4.10^{-3}	483	1101	42; 61		0.41; 0.43
	4.10^{-2}	525	1066	45; 46		0.43; 0.45
	50	(oscillations)	~1115	45		0.45
	110	(oscillations)	~1130	47		0.45
TD	4.10^{-4}	514	1170	43; 41	1.40 down to 1.26 (average 1.30)	(not available)
	4.10^{-3}	539	1162	43; 52		
	4.10^{-2}	554	1093	48; 50		
DD	4.10^{-4}	515	1149	48; 56	0.91	(not available)
	4.10^{-3}	545	1114	45; 52		
	4.10^{-2}	575	1086	59; 50		

The high levels of strain hardening, fracture strength and fracture elongation, typical of TWIP steels, are illustrated in Fig. 2 and Table 2. The strain rate sensitivity was negative at lower strain rates with the main contribution coming from work hardening. For higher strain rates, the sensitivity became positive. At room temperature, serrations were observed for strain rates lower than 4.10^{-2} s^{-1} and axial elongation higher than about 20%. For this reason, only values of strain averaged over the gauge part of smooth specimens are reported in the following. Some experimental scatter was found for yield strength (less than 8%) and tensile strength (less than 7%) due to strain instabilities. These were related to propagation of Piobert-Lüders-type bands along the gauge part of the tensile specimen [e.g. Allain et al, 2008]. Such phenomena are referred to as “dynamic strain ageing” (DSA) in the following. They induced strong variation in the values of Lankford coefficients. Consequently, some additional UT tests were carried out using the DIC technique to extract the Lankford coefficients reported in Table 2.

Anisotropy in strength was low (about 30 MPa) at the onset of plastic deformation, consistently with the very weak crystal orientation texture and morphological texture in this material. In a fine-grained Fe-22Mn-0.6C TWIP steel, [Barbier et al, 2009] showed that anisotropy increases with work hardening, due to the gradual development of texture components induced by both plastic slip and intensive twinning. Anisotropy in plastic strain was higher than that in strength.

For low strain rates, fracture occurred abruptly, right after propagation of a Piobert-Lüders-type band, probably somewhat before the Considère strain instability criterion was reached. This induced scatter in fracture elongation. For this reason, all available experimental values have been reported in Table 2.

At 400°C, strain hardening was still high but strength and fracture elongation were much lower than at room temperature. Pronounced necking occurred well before fracture, indicating a more stable ductile fracture process than at room temperature. No serration was detected in tensile curves. The strain rate sensitivity was negative for strain rates lower than 4.10^{-4} s^{-1}. At 400°C, pseudo-DSA is thus still present, in certain conditions, even if no mechanical twinning is expected to occur [e.g. Bouaziz et al, 2010]. Conversely, mechanical twinning may occur together with positive strain rate sensitivity (e.g.

for higher strain rates at room temperature, see Fig. 1b). Correlation between DSA and mechanical twinning is thus unclear in this material. There is yet a clear correlation between the occurrence of mechanical twinning and sensitivity to abrupt fracture.

3.2. Bauschinger effect

A strong Bauschinger effect was evidenced in shear loading (Fig. 3). It increased with increasing e_{max} (Fig. 3a). The kinematic contribution to hardening was about 50% of the applied stress, so that its evolution with e_{max} was not linear. This result is in agreement with those reported by [Bouaziz et al, 2008] in a vanadium-free Fe-22Mn-0.6C alloy. The contribution of isotropic hardening increased almost linearly with e_{max}, the slope being about 1740 MPa per unit strain (Fig. 3b).

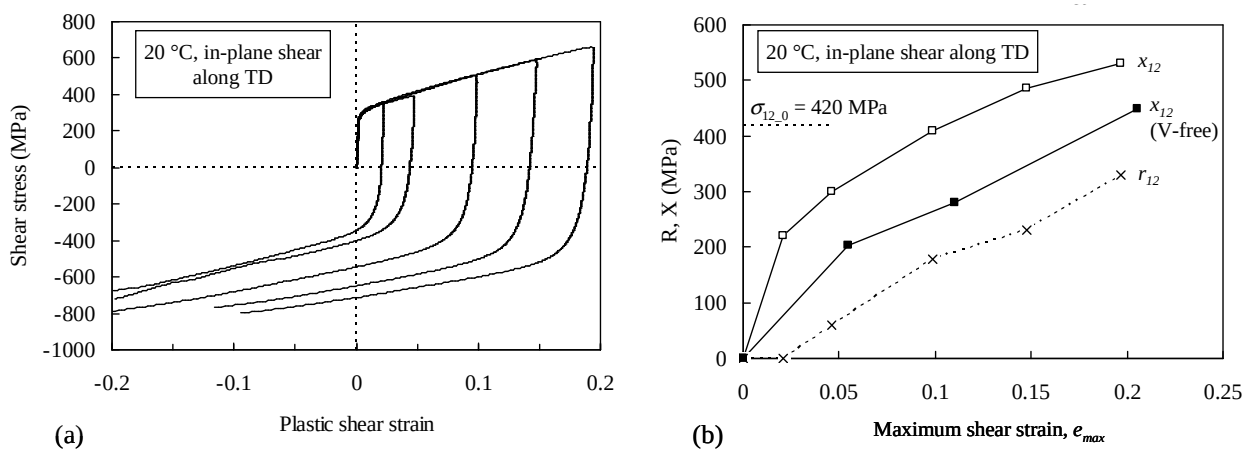


Figure 3: Room temperature shear test results. (a) Stress-strain curves; (b) respective contributions of kinematic (x_{12}) and isotropic hardening (r_{12}) to the shear stress. σ_{12_0} is the initial yield stress in these shearing conditions. Data for the vanadium-free alloy are taken from [Bouaziz et al, 2008].

3.3. Tensile behaviour of notched specimens

3.3.1. Double edge notched specimens

As in UT tests, only a slight anisotropy in strength and in fracture elongation was found with DENT specimens (Fig. 4a). The reproducibility of curves was better than 5 MPa (for a given notch opening) except for DENT05 specimens along TD, for which a difference by about 10 MPa was noticed for notch opening lower than 0.5 mm. Notch opening at fracture differed by less than 0.1mm between the two tests per condition. The notch radius did not significantly influence the load vs. notch opening curve (Fig. 4b) but strongly affected notch opening at fracture. No serration was detected in these curves. Constraints induced by the notches may have forced intense deformation bands, if any, not to propagate across the entire specimen. Although fracture occurred in an unstable manner, the DIC system was able to capture one image of a DENT05 specimen loaded at 0.5 mm.min^{-1}, with one crack initiated from each of the notch roots (Fig. 4c). The logarithmic reduction in thickness at fracture, evaluated in the SEM, was about -0.45±0.05 at each notch root, i.e., at crack initiation, and almost the same (-0.42 ±0.02) along the fracture ligament (representative of crack propagation). The values were identical to those measured in UT for strain rates higher than 4.10^{-2} s^{-1} (-0.45±0.01), whereas for lower strain rates (4.10^{-4} and 4.10^{-3} s^{-1}, respectively), the logarithmic reduction in thickness was slightly lower (-0.39±0.03 and -0.42 ±0.02, respectively).

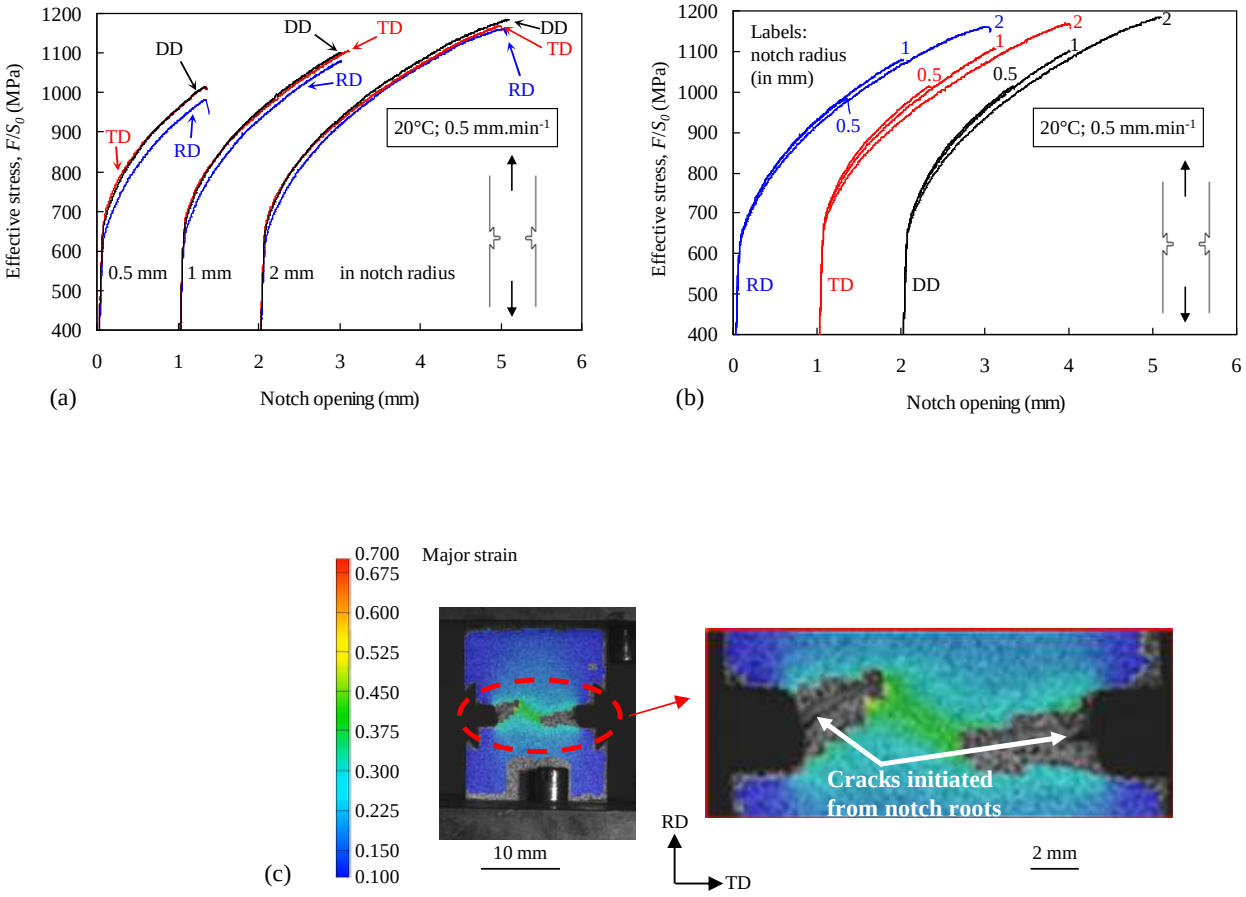


Figure 4: Plastic yielding and fracture of DENT specimens. (a,b) Effects of loading direction and notch radius (curves have been artificially shifted by 1 mm for better readability); (c) image captured with the camera showing cracks initiated from both notch roots (NT0.5 pulled along RD at 0.5 mm.min^{-1} superimposed to corresponding major (axial) engineering strain field measured by DIC.

3.3.2. Double edge notched shear specimens

The experimental behaviour of DENS specimens is reported in Fig. 5, together with model predictions that are introduced in Section 4. Load vs. notch opening curves of ungrooved DENS specimens (Fig. 5a) exhibited a slight upward curvature for displacements higher than about 3 mm. This was due to a gradual change in specimen geometry that induced stiffening (Fig. 5b). This was not observed by Brünig et al. [Brünig08], whose aluminium alloy did not exhibit the outstanding strain ability of TWIP steels. Anisotropy in strength was not negligible (about 6%). Significant rotation of the specimen was precluded by the fixture system. However, the bending stiffness of the machine was not high enough to suppress translation of the specimen ends perpendicular to the loading axis (Fig. 5b). At fracture, deformation was not constrained to the central part of the gauge region but extended from one notch root to the other, with a maximum value of about 0.4.

Grooved specimens fractured with much lower notch opening than ungrooved ones (Fig. 5c), and showed an anisotropy in strength of about 9%. Unlike for the other tests, specimens loaded along RD were slightly stronger than those loaded along TD. Fracture initiation occurred close to the centre (Fig. 5d) and strain was kept constrained between the grooves (Fig. 5d), with a maximum shear strain of about 0.59 at fracture. At the centre of the grooves, pure shear strain (at least from in-plane components) dominated throughout the test, so that this specimen was considered to be tested in conditions close to pure shear.

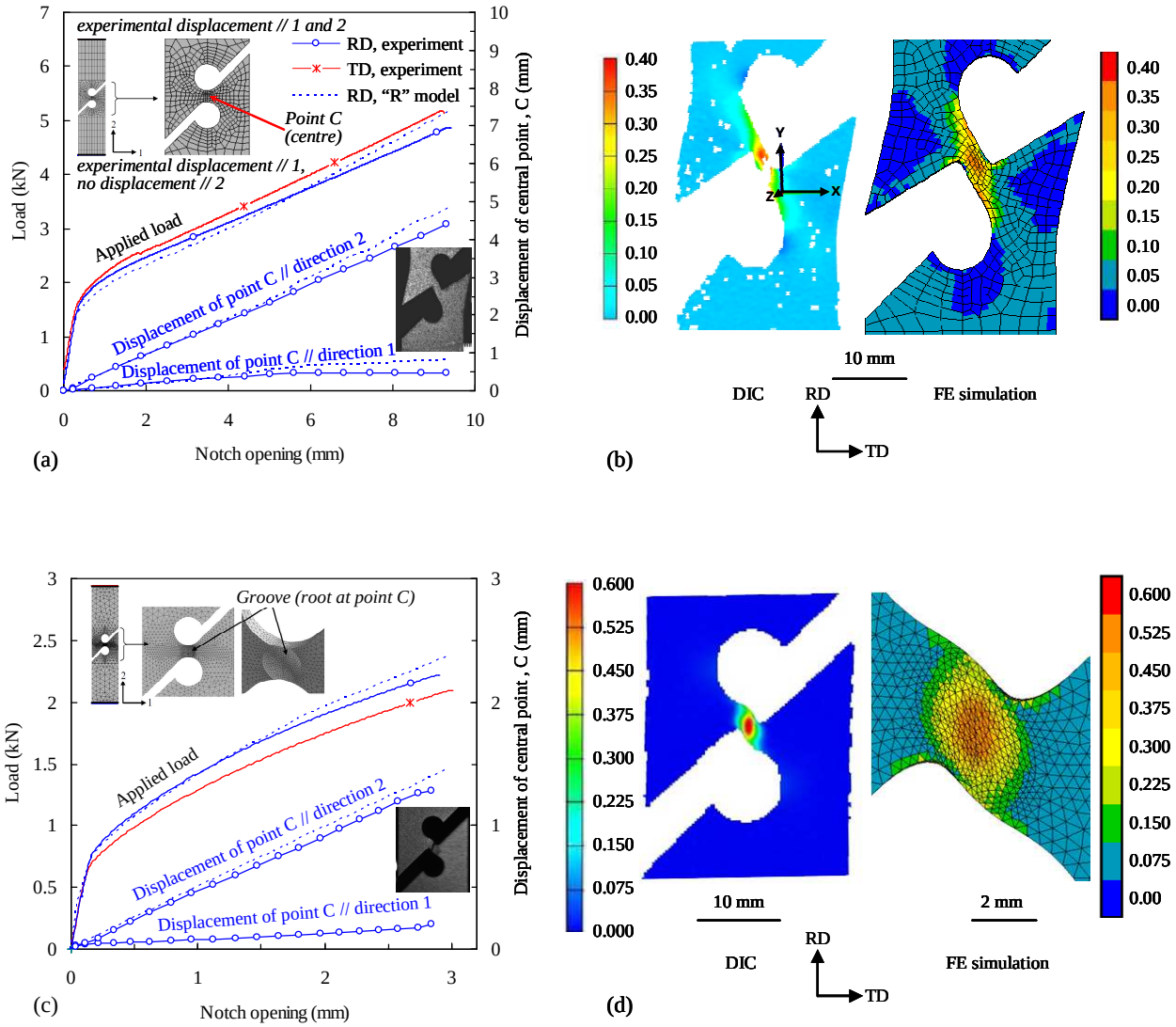


Figure 5: Results of tests on DENS specimens (continuous lines) compared to predictions of the "R" model (dotted lines). Load and displacement of central point vs. notch opening curves of (a) ungrooved and (c) grooved specimens (same curve labelling for (a) and (c)). Meshing with boundary conditions at specimen ends (displacement along directions 1 and 2) and appearance of specimen at fracture are shown as inlets. In-plane shear strain at fracture in specimens loaded along RD: DIC measurements and model predictions for (b) ungrooved and (d) grooved specimens.

3.3.3. Double side notched tensile specimens

The experimental behaviour of DSNT specimens is reported in Fig. 6, together with model predictions that are introduced in Section 4. Load vs. load line displacement curves (Fig. 6a) showed no change in curvature, a slight anisotropy in strength and, again, abrupt fracture with no detectable softening. The local behaviour (Fig. 6b) was determined by using an effective stress (i.e., load divided by specimen width and by the distance between notch roots along the sheet thickness, i.e. 1 mm) and by averaging axial elongation over the gauge region of DIC measurements (length 3.42 mm, centred at specimen centre). In the model, due to the mesh geometry, axial elongation was averaged over 3.50 mm. The slight difference (about 2%) between gauge length used in DIC measurements and in the model, respectively, is not expected to significantly affect the results. The crack propagated at about 47° from the loading axis (see inlet in Fig. 6b). Determination of fracture strain was out of reach of DIC measurements due to a limit in spatial resolution but it was higher than 0.3. With the spatial resolution

of DIC, strain localisation seems to have occurred between the two side notches (Fig. 6c). No variation in width was detected. The loading mode was thus close to generalised plane strain conditions.

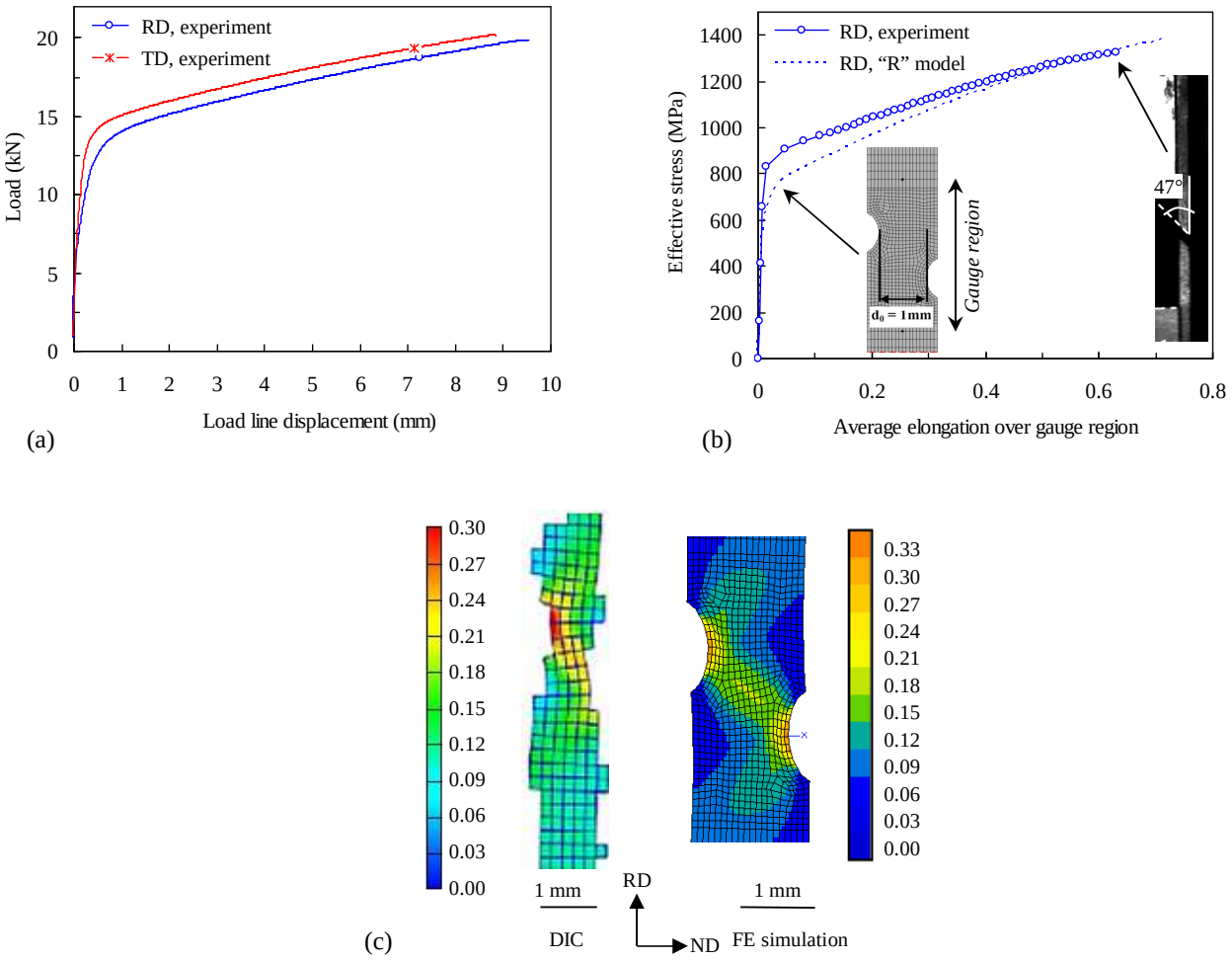


Figure 6: Results of tests on DSNT specimens. (a) Load vs. load line displacement curves; (b) Experimental and predicted effective stress vs. elongation curves (elongation averaged over 3.42 mm from DIC measurements and over 3.50 mm for model prediction), edge view of undeformed FE mesh and of fractured specimen; (c) major strain at fracture: DIC measurements and prediction of the "R" model (edge view).

3.4. Damage development and fracture mechanisms

Dimpled ductile fracture occurred for all specimens (Fig. 7). As already evidenced in this material [Lorthios et al, 2010, Xu et al, 2012], coarse cavities, strongly elongated along RD whatever the specimen geometry and loading direction, were found in fracture surfaces (Fig. 7a). Microtomography measurements [Lorthios et al, 2010] showed that (i) these cavities resulted from coalescence of smaller voids aligned along RD, (ii) their volume fraction was very low even close to the fracture surface (about 0.06% in average and locally not higher than 0.2% over 1mm from the fracture surface), and (iii) their anisotropic shape was consistent with plastic yield anisotropy as measured in UT with Lankford coefficients. They were mainly located between mid-thickness and quarter-thickness. A possible influence of the banded structure cannot be ruled out even if the distance between such coarse cavities (about 20-50 µm) does not scale with that between segregation microbands (a few µm, see Fig. 1b). No damage could be detected in any metallographic cross-section, even at the tip of arrested cracks (Fig. 7d).

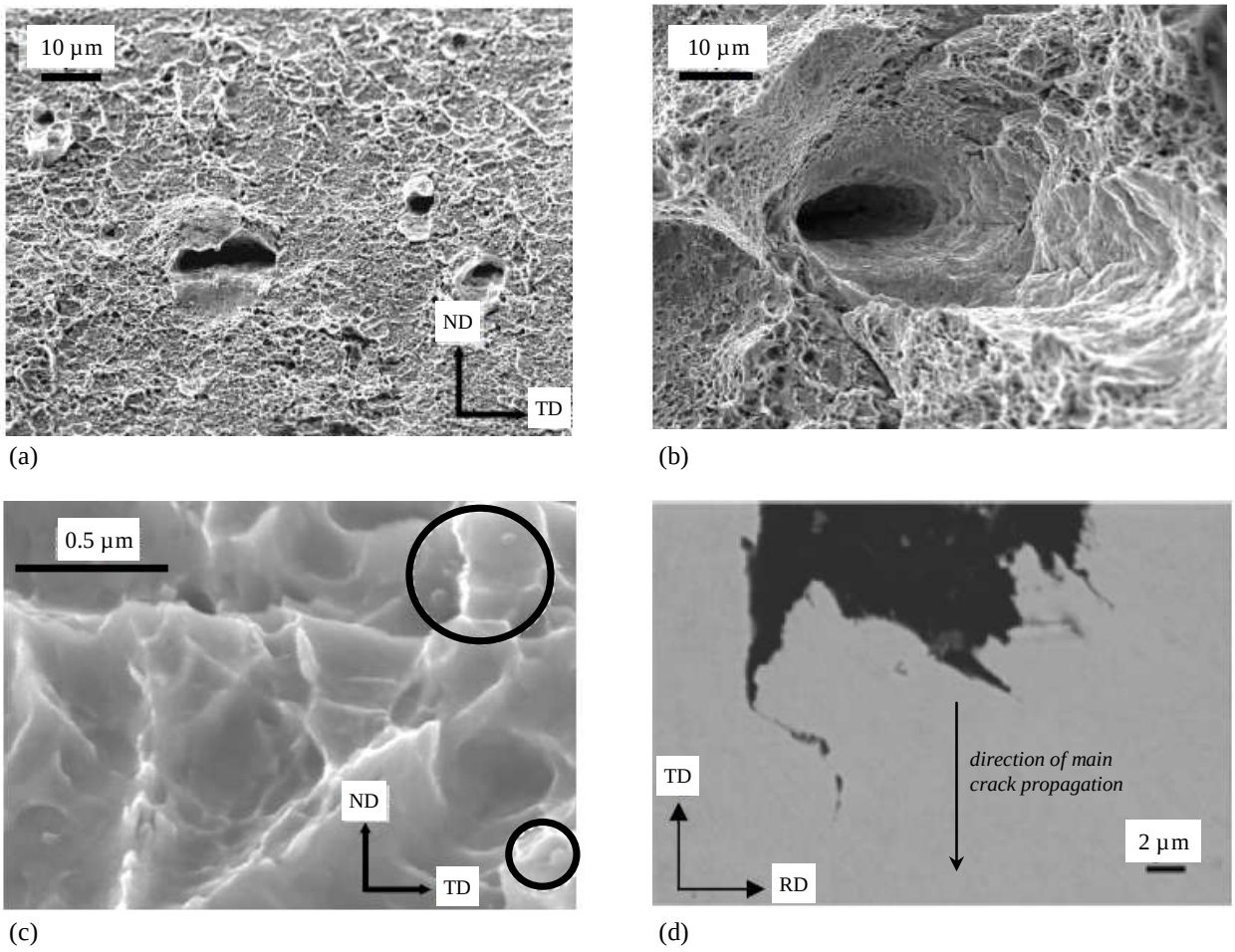


Figure 7: Fracture surfaces of specimens tested at room temperature with low loading rates. (a) Coarse cavities and finer dimples observed after UT along (a) RD and (b) DD directions. (c) Higher magnification view of smaller dimples with some tiny spherical particles indicated with black circles. (d) Tiny microcracks ahead of the crack tip in a cross-section of a Kahn specimen (test interrupted during stable crack propagation).

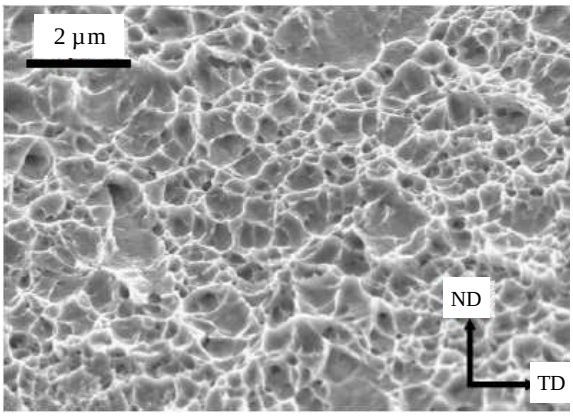


Figure 8: Fracture surface of a UT specimen pulled along RD at 110 s^{-1}.

Fracture surfaces mainly consisted of submicrometer-sized dimples (0.1-0.5µm in size), involving very limited void growth, as reported in literature [Bayraktar et al, 2004, Abbasi et al, 2009, Scavino et al, 2010, Chung et al, 2011] Consequently, void initiation mechanisms were difficult to observe. In some UT and DENS specimens, tiny spherical particles (about 40 nm in diameter) were found inside dimples (Fig. 7c). Their size was compatible with the size distribution of vanadium carbides (VC) in vanadium bearing Fe-22Mn-0.6C austenitic steels [Dumay, 2008], with particles having an average diameter of 7 nm, 3% of the particles being in the range 20-60 nm. In a vanadium-free material, larger dimples of about 1-2 µm in size were found instead [Allain, 2004].

To determine whether void nucleation in the investigated material could entirely be attributed to VC particles higher than about 20 nm in size (i.e. to about 3% of the VC particles), the number density of these particles was roughly estimated. It was assumed that almost all vanadium atoms were trapped into stoichiometric (NaCl type) precipitates. The number density of precipitates was estimated by considering that all precipitates had the same diameter (7 nm). Then, by only considering 3% of these particles, the distance between coarser precipitates was calculated to about 30 µm. Even if strong approximations were made in this simple model because the actual size and spatial distributions of VC particles were not known, such a distance is by far higher than the size of finer dimples in Fig. 7. This suggests that voids could initiate from either much finer precipitates that could not be imaged in the SEM, or even elsewhere, owing to e.g. complex interactions between carbides and mechanical twins. Even if cross-section observations in the TEM would be possible by taking a thin foil close to the fracture surface (e.g. by focused ion beam milling techniques), further deformation due to void coalescence may have strongly modified the deformation microstructure (dislocation distribution and microtwins) after dimple nucleation.

Fracture surfaces of specimens tested at room temperature were similar whatever the elongation rate (Fig.7, Fig. 8), hence, whatever the strain rate sensitivity (Fig. 5). This suggests that the void nucleation and coalescence mechanisms are not significantly affected by the strain rate sensitivity, possibly because intense strain localisation induces high strain rates at a very local scale, whatever the loading conditions applied in the present study.

At 400°C, slant fracture was also observed. Primary dimples were more widely open than at 20°C (Fig. 9). The origin of these elongated cavities was clearly evidenced to be coalescence of smaller, aligned cavities as already observed at room temperature. Finer dimples were significantly larger (more than 1 µm in average size) than those found at room temperature (compare Fig. 7 with Fig. 9). This confirms that despite its negative strain rate sensitivity (at least for low elongation rates), the considered material was less sensitive to strain localisation at 400°C than at room temperature.

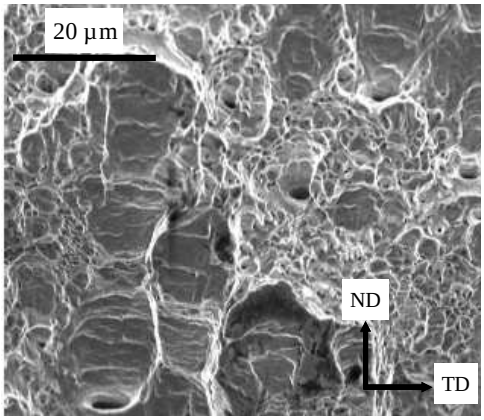


Figure 9: Fracture surface after UT testing at 400°C along RD: coarser cavities and finer dimples.

4. Mechanical analysis of experiments and derivation of a fracture criterion

To derive a fracture criterion from available experimental data, stress and strain fields had to be determined at fracture initiation as accurately as possible. To this aim, mechanical analysis of all tests was carried out by using a finite element approach using the general purpose, implicit code "Z-set" [Besson and Foerch, 1997]. As physical mechanisms of fracture initiation were still unclear, a phenomenological model was selected. Unlike recent micromechanical approaches [Allain et al, 2004, Bouaziz et al, 2008, Gil Sevillano, 2009, Soulami et al, 2011, Favier and Barbier, 2012, Steinmetz et al, 2013], and unlike models based on dislocation and twinning theory (e.g. [Liu et al., 2015]), the constitutive behaviour of this material was also described using a phenomenological approach to provide a unique framework for plastic flow and fracture modelling. The DSA phenomenon was not taken into account in this model. As fracture occurred abruptly at room temperature, without significant softening or extended damage development, only a fracture initiation criterion was considered. No coupling between plastic yield and damage development was thus introduced in the model.

4.1. Constitutive equations

From experimental results, anisotropy in strength appears from the beginning of plastic yielding and gradually develops, so that it was chosen to represent it by an anisotropic yield criterion, together with either only isotropic ("R" model) or mixed isotropic and kinematic ("R + X" model) contributions to hardening. Isotropic elastic properties were assumed (Young's modulus of 170 MPa and Poisson ratio of 0.3). Three yield criteria were considered, namely, a von Mises yield criterion, the anisotropic criterion developed by Barlat et al. [Barlat et al, 1991] and the Bron-Besson anisotropic yield criterion [Bron and Besson, 2004]. Full identification of constitutive parameters and numerical simulation of all tests showed very similar results for the two anisotropic criteria, so that only results obtained using the criterion by [Barlat et al., 1991] are reported here. Isotropic hardening was described using a Voce-type formulation; description of kinematic hardening was derived from the Armstrong-Frederick formulation. Note that such a model has already been used to describe the anisotropic plastic flow in various materials under complex loading paths [Laurent et al, 2009; Shinohara et al, 2010; Vladimirov et al, 2010]. In the following, the reference frame is that defined by RD, TD and ND. All calculations were carried out using a finite strain framework but for the sake of simplicity, model equations presented below are expressed using small strain formalism. The finite strain formulation adopted in this work was based on the use of a local objective frame as proposed in [Besson et al., 2009]. Observer invariant stress and strain rate measures were defined by transport of the Cauchy stress and strain rate into the corotational frame characterized by rotation Q (function of both space coordinates and time).

In this model, following [Barlat et al, 1991], a linear transformation (fourth-order tensor, $\underline{\underline{S}}$) was used to define a modified deviator $\underline{T}_{dev}$ of any second-order tensor $\underline{T}$; for a symmetric tensor $\underline{T}$, $\underline{T}_{dev}$ is expressed as follows using Voigt notations:

$$\underline{T}_{dev} = \underline{\underline{S}} : \underline{T} \text{ , with } \underline{\underline{S}} = \begin{pmatrix} \frac{c_2+c_3}{3} & -\frac{c_3}{3} & -\frac{c_2}{3} & 0 & 0 & 0 \\ -\frac{c_3}{3} & \frac{c_1+c_3}{3} & -\frac{c_1}{3} & 0 & 0 & 0 \\ -\frac{c_2}{3} & -\frac{c_1}{3} & \frac{c_1+c_2}{3} & 0 & 0 & 0 \\ 0 & 0 & 0 & c_4 & 0 & 0 \\ 0 & 0 & 0 & 0 & c_5 & 0 \\ 0 & 0 & 0 & 0 & 0 & c_6 \end{pmatrix} \quad (1)$$

In Eq. (1), c_i (i = 1-6) are adjustable material parameters that are linked to the (RD,TD,ND) reference frame. The anisotropic scalar measure, T_B, of tensor $\underline{T}$ is a function of the eigenvalues $\underline{T}_1^{dev} \geq \underline{T}_2^{dev} \geq \underline{T}_3^{dev}$ of $\underline{T}_{dev}$, with a an adjustable material parameter:

$$T_B = \frac{1}{2}\left(\left|T_1^{dev} - T_2^{dev}\right|^a + \left|T_2^{dev} - T_3^{dev}\right|^a + \left|T_3^{dev} - T_1^{dev}\right|^a \right)^{1/a} \tag{2}$$

The viscoplastic potential is a function of the stress tensor, $\underline{\sigma}$, the kinematic contribution to hardening, $\underline{X}$, and the isotropic contribution to hardening, R, as follows:

$$f\left(\underline{\sigma}, \underline{X}, R\right) = \left(\underline{\sigma} - \underline{X}\right)_B - R \tag{3}$$

The viscoplastic strain rate tensor, $\underline{\dot{\varepsilon}}_p$, is calculated using a normality rule on function f, together with a power-law flow equation for the viscoplastic strain rate, $\dot{p}$:

$$\underline{\dot{\varepsilon}}_p = \dot{p}\frac{\partial f}{\partial \underline{\sigma}} \text{ with } \dot{p} = \dot{\varepsilon}_0\left(\frac{\max\left(0, f\right)}{\sigma_0}\right)^n \text{ and } \dot{\varepsilon}_0 = 1 \text{ s}^{-1}. \tag{4}$$

In Eq. (4), σ_0 and n are constitutive material parameters.

Isotropic hardening is a function of the cumulative viscoplastic strain, p, using a linear term and a non-linear term (Voce-type):

$$R = R_0 + H\ p + Q\left(1 - \exp\left(-bp\right)\right) \tag{5}$$

For the "R+X" model, the kinematic contribution $\underline{X}$ to hardening is given by the additive combination of a linear term $\underline{X}_1$ and a non-linear term $\underline{X}_2$, as follows:

$$\underline{X} = \underline{X}_1 + \underline{X}_2 \tag{6}$$

$$\underline{\dot{X}}_1 = \frac{2}{3}C_1\underline{\dot{\alpha}}_1 \text{ with } \underline{\dot{\alpha}}_1 = \underline{\dot{\varepsilon}}_p \text{ for the linear term, and} \tag{7}$$

$$\underline{\dot{X}}_2 = \frac{2}{3}C\underline{\dot{\alpha}}_2 \text{ with } \dot{\alpha}_2 = \underline{\dot{\varepsilon}}_p - \dot{p}D\underline{\alpha}_2 \text{ for the non-linear term.} \tag{8}$$

It was not possible to satisfactorily represent reverse shear test results using constant values of C and D, so that heuristic evolutionary equations were proposed as follows:

$$C = \frac{3}{2}C_0\frac{D}{D_0} \text{ and } D = D_0 + \left(D_1 - D_0\right)\left(1 - \exp\left(-\frac{p}{p_0}\right)\right) \tag{9}$$

In Eq. (9), C_0, D_0, C_1, D_1 and p_0 are material parameters.

The total number of parameters for the "R" model is 13: 7 for the viscoplastic potential, 2 for the viscoplastic flow rule, and 4 for isotropic hardening. Five additional parameters are needed to describe kinematic hardening in the "R+X" model.

4.2. Identification of constitutive parameters

Identification of constitutive parameters was based on quasistatic uniaxial tension results (tensile curves as well as Lankford coefficients, one test per direction i.e. 3 tests), reverse shear tests (5 tests) and load vs. notch opening curves for the DENT specimens (9 tests: 3 per direction, 3 per notch geometry). UT and reverse shear tests were modelled using a single representative volume element. DENT specimens were meshed in three dimensions by considering one-eighth of each specimen with usual symmetry conditions. Linear eight-node bricks with full integration were used with a mesh size fine enough for the load vs. notch opening curves to be represented without any dependence on the size of finite elements. To account for the very low strain rate sensitivity of the material, low values were fixed for both σ_0 and n, to keep a negligible viscous contribution to stress while facilitating integration of constitutive equations with respect to an elastic-plastic formulation. An implicit integration scheme was used for all calculations. In absence of experimental results involving mainly loading along ND, the values of c_5 and c_6 were arbitrarily set to 1.0. Remaining material parameters were optimised using a Levenberg-Marquardt algorithm. The resulting sets are reported in Table 3.

Table 3: Optimised sets of constitutive parameters for the "R" and "R+X" models.

	Modulus		Anisotropic yield potential							Flow rule		Isotropic hardening				Kinematic hardening				
	E (GPa)	ν	a	c_1	c_2	c_3	c_4	c_5	c_6	σ_0 (MPa)	n	R_0 (MPa)	H (MPa)	Q (MPa)	b	C_0 (MPa)	C_1	D_0	D_1	p_0
"R" model	170	0.3	9.95	1.15	1.08	1.12	1.16	1.0	1.0	1.0	5.0	602	595	2037	2.38	...	...	...	...	...
"R+X" model	170	0.3	9.95	1.15	1.08	1.12	1.16	1.0	1.0	1.0	5.0	492	258	1777	2.58	44817	829	349	70	0.015

The value of parameter a was obtained by numerical fitting. It is higher than the value of 8 that is recommended for in-plane loading of face-centred cubic structures by [Hosford, 1979, Hosford, 1985]. This value of 8 was fitted to upper-bound calculations of yield loci, assuming rotationally symmetric textures and conventional slip systems. The general method is described in detail in [Logan and Hosford, 1980]. As the considered TWIP steel was processed by a rolling + annealing schedule, rotational symmetry in crystal texture cannot be assumed in the present case. Moreover, twinning should be taken into account as a significant deformation mechanism in this material.

The yield locus, expressed by normalising stresses with respect to the yield stress under uniaxial tension along RD, has been plotted in Fig. 10 with those from [Chung et al., 2011, Xu et al., 2012]. For comparison purposes, the yield locus identified by [Busch et al., 2014] on a so-called TWIP/TRIP steel is also added. The higher value of parameter a in the present study leads to a less rounded shape of the yield surface (note that a value of $a = 4$ yields to an ellipse). The main point, here, is the lower symmetry (with respect to the ($\sigma_{RD} = \sigma_{TD}$) axis) of the curve from the present model, compared with the other three ones. This is linked to the set of optimised parameters c_i describing the anisotropic yield potential.

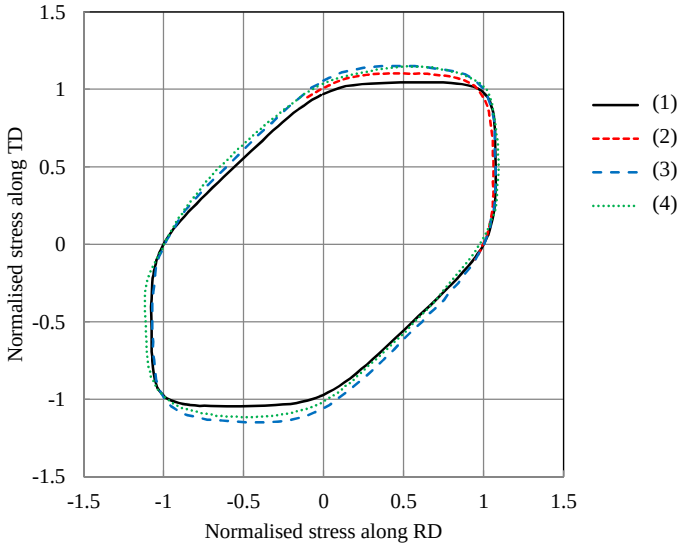


Figure 10: In-plane yield locus predicted from the present study (1), compared with those from literature data: (2) [Chung et al., 2011]; (3) [Xu et al., 2012]: (4) [Busch et al., 2014]. Stresses along RD and ND have been normalised by the yield stress under uniaxial tension along RD.

The UT behaviour is well described by the model, namely, within a relative error in strength of 5-7% for an elongation of 10%; this difference decreases with increasing elongation down to less than 1% at fracture. For a given elongation, lateral strain was only slightly overestimated (relative difference lower than 4%) and slightly underestimated (relative difference lower than 2%) for tests along RD and TD, respectively, so that strain anisotropy was well reproduced. The relative difference between measured and predicted load vs. notch opening curves of DENT specimens was lower than 6%, and better than 4% for a notch opening lower than 1 mm. The loading part of reverse shear tests was well described using the model, while isotropic hardening was obviously overestimated in the unloading part. Predictions of the "R+X" model were much closer to experimental measurements for this test, yet at the expense of accuracy in strain anisotropy under uniaxial tension (lateral strain overestimated by 7% and underestimated by 6% for tests along RD and TD, respectively). From Figs 5 and 6, load vs. displacement curves, as well as local strains close to the fracture locus for the last recorded experimental data before fracture, are very satisfactorily described with the "R" model. The "R+X" model is thus significantly more accurate than the "R" model only if unloading (or significant change in the loading mode) occurs during the tests.

4.3. Strain paths and estimated stress state at fracture initiation

4.3.1. Determination of fracture initiation conditions with the "R" model

Due to marked instability at high strains, UT specimens were not considered in the analysis of fracture initiation conditions. In fact, strain localisation bands induce local stress concentrations that require taking pseudo DSA and strain rate sensitivity into account to be properly described [Lorthios, 2011]. Here, focus was made on a model that is more easily usable in forming applications. Numerical simulation of tests on notched specimens were carried out using refined meshes (typical size of elements close to the notch root: 0.1 mm in the sheet plane and 0.2 mm along ND), in order to obtain accurate values of stress and strain fields close to fracture initiation sites.

Ungrooved DENS specimens were meshed using quadratic brick elements with reduced integration (mesh size 0.55 mm in the sheet plane, 0.5 mm along ND). Grooved DENS specimens were meshed

with quadratic tetrahedral elements with reduced integration (element size in the gauge part: 0.16 mm in the sheet plane, 6 elements along ND). Displacement was prescribed along both RD and TD according to experimental measurements at the edges of the DIC window, close to the specimen fixtures (see inlets in Fig. 5). This allowed taking the bending stiffness of the load line into account.

DSNT specimens were modelled using quadratic brick elements with full integration. The size of elements in the notched part was 0.7 mm in the (RD,ND) plane. As the reduction in width was negligible in DSNT tests, the size of the elements was reduced down to 1 mm along TD together with generalised plane strain conditions (i.e., homogeneous value of deformation along TD for any slice of the specimen perpendicular to TD).

For all of these tests, load vs. displacement curves and strain fields were in very good agreement with experimental data (Figs 4, 5, 6).

The value of the stress triaxiality ratio η_B (i.e. the ratio of the hydrostatic stress, ξ, to the anisotropic equivalent stress, σ_B), the equivalent strain p (here denoted as ε_B to explicitly make reference to the Barlat yield criterion), the ratio of minor to major strain α_B, were determined at integration points that were closest to the fracture initiation site, for the same value of displacement as that experimentally observed at fracture. The values are reported in Table 4. For DENT specimens, the values were taken at the notch root, at mid-thickness. For ungrooved DENS specimens, the values of α_B taken at the edge and at the centre of the notched region are very different, evidencing a strong gradient in α_B. As the fracture initiation point could not be experimentally determined, these specimens were not used for quantitative determination of the fracture criterion. For grooved DENS specimens, the values were taken at mid-thickness, between the groove roots. Except for the DSNT specimen, the value of α_B at the fracture initiation point remained almost constant throughout the test. For the DSNT specimen, α_B started from near zero up to a cumulative strain of about 0.1 and then turned into -0.18. Such a nearly radial strain path was not the case, however, everywhere in the tested specimens: the high deformability of the TWIP steel led to a noticeable change in specimen geometry before fracture. For instance, in the central region of DENT specimens, a transition from plane strain tension toward uniaxial tension occurred during stress redistribution. Consequently, the stress and strain conditions *at fracture* were the same whatever the notch radius, yet with avoiding macroscopic strain instability observed in uniaxial tension. The DENT geometry could thus be regarded as useful to investigate fracture initiation under nearly uniaxial tension for such ductile materials exhibiting strain instabilities.

As global load vs. displacement curves were well predicted with the “R” model, and due to nearly constant values of α_B at the fracture initiation point, it was decided to only use the “R” model to derive a fracture initiation criterion. In the following, data processed with the “R” model will be denoted as “experimental”, in the forming limit diagram. They are reported with symbols in Fig. 11.

Table 4: Characteristic values of stresses and strains at fracture initiation estimated with the "R" model, compared to experimental data. α is the ratio of minor to major strain. All specimens are loaded along RD. Superscripts * and *a* denote tests results from [Dell and Gese, 2007] (also reported in [Bouaziz et al, 2011]) and internal ArcelorMittal tests [Bouaziz et al, 2011], respectively.

Specimen	Logarithmic strain along ND: experiment / model prediction	Strain ratio, α_B	σ_B (MPa)	η_B	ρ_B (MPa)	Lode angle, θ_B (rad)	ε_B	τ_{max} (MPa)
UT	-0.39	-0.47	2584	0.29	2277	0	0.65	1138
DENT05	-0.45 / -0.37	-0.48	2470	0.362 down to 0.306	2176	0	0.62	1126
DENT1	-0.45 / -0.37	-0.46	2494	0.330 down to 0.300	2197	0	0.60	1102
DENT2	-0.45 / -0.37	-0.45	2557	0.300 down to 0.295	2253	0	0.57	1076
DENS, ungrooved	Fracture initiation point not well localised	-0.47 (edge), -1 (centre of gauge part)		0				
DENS, grooved	-0.59 / -0.58	-1	2357	0	2077	$\pi/6$	0.52	1089
DSNT	not available / -0.37	-0.18	2124	0.38	1871	0.41	0.41	1014
Center hole tensile*	-0.34	-0.50^{VM}	2443	0.29	2152	0	0.56	1076
Plane strain*	-0.39	0^{VM}	2032	0.42	1790	0.48	0.38	957
Tilted plane strain*	-0.30	-0.20^{VM}	1916	0.35	1688	0.32	0.33	885
Equibiaxial stretching*	-0.75	1^{VM}	2615	0.60	2304	$\pi/3$	0.66	1189
Shear*	$\varepsilon_{12} = 0.48$	-1^{VM}	2221	0	1957	$\pi/6$	0.46	1026
Marciniak 1[a]	-0.41	0.08 (exp. value)	2028	0.56	1787	0.61	0.38	956
Marciniak 2[a]	-0.64	0.68 (exp. value)	2446	0.60	2155	0.95	0.57	1103

4.3.2. Influence of anisotropic plastic yield on macroscopic fracture initiation conditions

To quantify the difference between fracture initiation conditions determined using such a complex "R" model and those determined from much simpler, more commonly used modelling, the UT test along RD with an elongation rate of 4.10^{-4} s^{-1} was modelled with a von Mises yield criterion and a Hollomon-type evolutionary equation of the flow stress:

$$\sigma = K_H \, \varepsilon_p^{n_H} \, , \qquad (10)$$

ε_p being the von Mises equivalent plastic strain (equal to the uniaxial plastic strain, in uniaxial tension, with the von Mises yield criterion). The fitted values of K_H = 2605 MPa and n_H = 0.43 allowed accurate prediction (better than 2% difference in strength) of the tensile curve for strains higher than about 0.1 (which is much lower than the fracture strain). This model, denoted as "VM-H" in the following, was used to analyse the same experimental database, using the same numerical procedure as for the "R" model except for the constitutive behaviour.

At fracture, compared to the more accurate "R" model, the "VM-H" model overestimates the value of stress triaxiality by 10%, and the value of cumulative plastic strain by 10 to 20% (in relative error values). It underestimates the value of equivalent stress (compared to that of σ_B) by about 200 MPa. Thus, taking anisotropic yielding into account is essential to accurately determine fracture initiation conditions for this material. Consequently, only values determined with the "R" criterion are considered in the following.

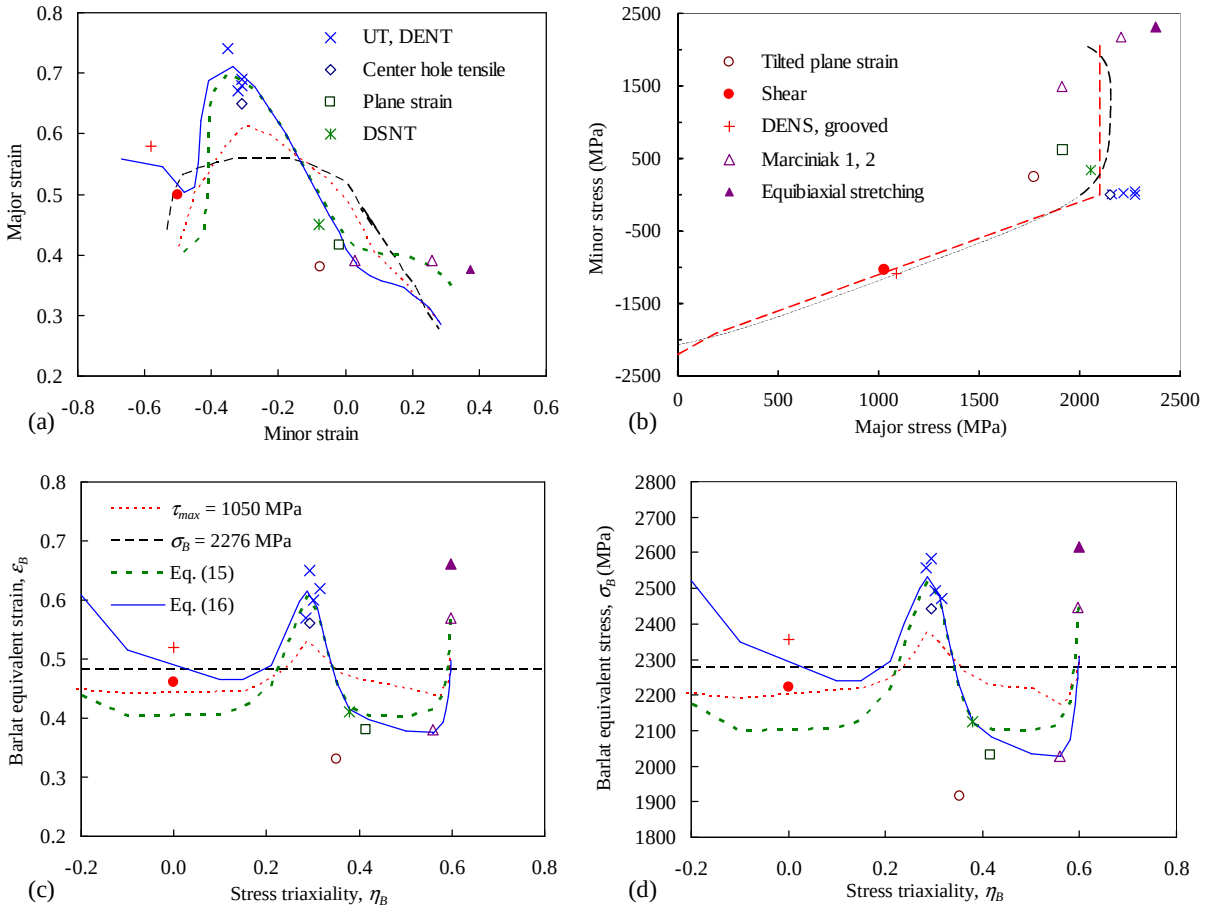


Figure 11: Experimental determination (symbols) and prediction (lines) of the FLD of the Fe-22Mn-0.6C-0.2V TWIP steel (main loading along RD). (a) Major vs. minor strains; (b) minor vs. major stresses; (c) equivalent strain vs. stress triaxiality; (d) equivalent stress vs. stress triaxiality. All quantities are evaluated using the "R" model. Same labelling for (a-d).

4.3.3. "Experimental" forming limit diagram

To complete the experimental database of the previous section, the results of additional mechanical tests carried out using the same material were also processed using the "R" model to extract fracture initiation conditions for a wider range of loading paths [Dell and Gese, 2007, Bouaziz et al, 2011]. The experimental procedure is reported in [Hooputra et al, 2004, Dell et al, 2008] and results are also reported in Table 4. They included Marciniak-type forming tests with two different values of strain ratio α (experimentally measured from optical strain field monitoring) [Bouaziz et al, 2011], and a series of tests [Dell and Gese, 2007] involving plane strain tension with a double side notched tensile specimen, equibiaxial stretching, uniaxial tension of a 20-mm-wide, 110-mm-long rectangular specimen bearing a central hole of 10 mm in diameter, shear loading of a specimen with two side groves, and "tilted plane tension" of a specimen with two side groves (in front of each other), perpendicular to the sheet thickness and making a 45° angle (in the sheet plane) with the RD loading direction. To process these additional data while minimising numerical issues such as contact between tooling and specimens, these tests were simulated using a single representative volume element with prescribed value of α. This value was determined experimentally for the Marciniak-type tests. An approximation with analytical formulae using a "VM-H" assumption was made for the tests from [Dell and Gese, 2007].

4.4. Fracture initiation criterion

The fracture initiation criterion was determined from the above mentioned tests that involve nearly constant strain paths and loading along RD. The following results, therefore, should not be directly applied to complex loading paths encountered in forming operations.

As reported by [Wierzbicki et al, 2005, Zadpoor et al, 2009] in an aluminium alloy sensitive to shear fracture, a criterion based on the maximum shear stress, τ_{max}, may in certain cases represent the fracture FLD with good accuracy based on a minimum number of calibration tests. In the present case, Fig. 11a and Tables 4 and 5 show that a critical value of either σ_B (as determined using the "R" model), or of the maximum shear stress, τ_{max}, cannot represent the "experimental" forming limit diagram with an accuracy better than 10% and ±7%, respectively. Such a critical shear stress was mentioned, but not used by [Xu et al, 2012]. In a Fe-22Mn-0.6C-0.2V TWIP steel, a critical shear stress of 1015 MPa, determined from a variety of mechanical tests analysed using a "VM-H" model, allowed a prediction of the FLD with an accuracy better than about 20% [Bouaziz et al, 2011]. In spite of the ductile fracture mode, void growth is very limited even for high values of stress triaxiality ratio so that criteria such as those of [McClintock, 1968, Rice and Tracey, 1969, Oyane et al, 1980] are not relevant for this material. The candidate fracture criterion should be able to address a wide range of values for stress triaxiality ratio η, including those close to zero. To this aim, criteria developed for modelling either rock fracture or fracture of metal alloys very sensitive to shear fracture (even if less ductile than TWIP steels) were considered.

The stress state was expressed in terms of Haigh-Weestergaard (or Lode) coordinates in the space of maximum principal stresses as in [Fricker and Meckbach, 1999, Xue and Wierzbicki, 2008, Bai and Wierzbicki, 2010]. The first invariant I_1^B of the stress tensor calculated with the "R" model at fracture initiation, $\underline{\sigma^B}$, and the second and third invariants, J_2^B and J_3^B, of the modified deviator $\underline{\sigma_{dev}^B}$, were first calculated. Superscript "B" denotes that unlike in e.g. [Bai and Wierzbicki, 2010], the fracture criterion was set by using the same "R" model (including the Barlat-type yield criterion) as that used to extract fracture initiation conditions from experimental data. Note that such expression "loses" the actual loading axes with respect to the principal directions of the sheet material. In other words, the forming limit diagram (FLD) cannot be uniquely expressed as a function of the invariants of stress tensors, as for an isotropic material. As a consequence, only data of tests involving loading along RD were considered with the exception of shear, for which principal strains are rotated with respect to the

(RD, TD) frame. Results of shear tests will thus be only qualitatively interpreted here. The FLD determined in this study will be termed the "RD-FLD" to denote loading along RD. Great care must thus be taken when using this RD-FLD for more complex loading paths (or even loading along other directions) such as in forming conditions. Although being less accurate, a FLD determined using an isotropic (e.g. von Mises) yield criterion overcomes this difficulty.

For the above mentioned invariants, and for a von Mises yield criterion, Haigh-Weestergard coordinates are expressed as follows:

$$\xi^{VM} = \frac{I_1^{VM}}{\sqrt{3}} \; ; \; \rho^{VM} = \sqrt{2J_2^{VM}} \; ; \; \cos\left(3\theta^{VM}\right) = \frac{3\sqrt{3}}{2}\frac{J_3^{VM}}{\left(J_2^{VM}\right)^{3/2}} \text{ being the Lode parameter.} \tag{11}$$

With using the "R" model, the definition of ξ, denoted here as ξ^B was not changed but the values of ρ and Lode angle θ were modified to be consistent with the formalism of constitutive equations. The value of ρ^B was taken proportional to the anisotropic measure of stress, σ_B, and equal to the value of uniaxial fracture stress $\sigma^B_{UT//RD}$ in the case of uniaxial tension (again, along RD):

$$\rho^B = \sigma^B_{UT//RD} = \frac{\sigma_B}{k_{UT//RD}} \text{ with } \; k_{UT//RD} = 1.135 \text{ from numerical simulation of UT along RD.} \tag{12}$$

For the von Mises yield criterion, the Lode parameter may be defined either using the stress tensor as in Eq. (11), or using the strain rate tensor $\underline{\dot{\varepsilon}}_p^{VM}$ and the plastic strain rate, $\dot{p}^{VM}$, as follows:

$$\cos\left(3\theta_\varepsilon^{VM}\right) = 4\frac{\det\left(\underline{\dot{\varepsilon}}_p^{VM}\right)}{\left(\dot{p}^{VM}\right)^3} \tag{13}$$

With the yield criterion used in the "R" model, definitions of the Lode parameter based respectively on the stress and on the strain rate tensors are not equivalent. As the considered material is very sensitive to strain localisation, the strain-rate based definition was chosen to represent a strong local variation in strain rate (but not a discontinuity as in [Rudnicki et al, 1975, Needleman and Rice, 1978]). Coefficient $k_{UT//RD} = 1.135$ was again introduced in the definition of the Lode parameter to ensure that the resulting value ranges between (-1) and (+1). Consequently, the Lode angle θ_ε^B was defined as follows:

$$\cos\left(3\theta_\varepsilon^B\right) = \frac{4}{k^3_{UT//RD}}\frac{\det\left(\dot{\varepsilon}_p^B\right)}{\left(\dot{p}^B\right)^3} \tag{14}$$

As a first approximation, inspired by very limited void growth in this material, the fracture criterion was tentatively described as a function of ρ^B and θ_ε^B, i.e., the influence of hydrostatic pressure was neglected. The simplest possible function of these two variables that could reasonably account for experimental data was that of a semi-elliptical cylinder in the Haigh-Weestergaard coordinates:

$$f^B\left(\underline{\sigma}\right) = \left(\frac{\rho^B}{a^B}\right)^2 \cos^2\left(3\theta_\varepsilon^B\right) + \left(\frac{\rho^B}{b^B}\right)^2 \sin^2\left(3\theta_\varepsilon^B\right) - 1 = 0 \tag{15}$$

The value of a^B was fitted to 2200 MPa by averaging values obtained from uniaxial and equibiaxial tension tests with $\sin(3\theta_\varepsilon^B) = 0$. The value of b^B was fitted to 1850 MPa, by averaging values obtained from shear and plane strain tests with $\sin(3\theta_\varepsilon^B)$ close to 1 (exactly 1 for shear, ≈ 0.99 for plane strain tension). Thus, four tests were used to identify this fracture criterion. The FLD was then estimated using this criterion for a variety of loading conditions as reported in Fig. 11. Using such a function remarkably improves the prediction of fracture with respect to the criteria based on either σ_B or τ_{max}. However, Eq. (15) underestimates the resistance to fracture in shear and overestimates it for

plane strain tension, by making a compromise between these two tests, for which $\sin\left(3\theta_\varepsilon^B\right) \cong 1$. Such a difference between these two experimental results could arise from (i) the direction of principal strains being different from the RD, TD, ND directions or (ii) a possible effect, yet rather weak, of hydrostatic pressure. The latter effect could be simply taken into account by introducing a weak dependence on ξ. This was done using a linear function, the fracture criterion becoming a cone, with apex at ($\xi = \xi_0$, $\rho = 0$) and aperture angle $\tan^{-1}(h^B)$:

$$g^B(\underline{\sigma}) = \left(\frac{\rho'^B}{a'^B}\right)^2 \cos^2\left(3\theta_\varepsilon^B\right) + \left(\frac{\rho'^B}{b'^B}\right)^2 \sin^2\left(3\theta_\varepsilon^B\right) - 1 = 0 \text{ with } \rho'^B = \frac{\rho^B}{h^B\left(\xi_0 - \xi^B\right)} \quad (16)$$

Parameters h^B and ξ_0 were identified in the ($3\theta_\varepsilon^B \cong \pi/2$) section using plane strain tension and shear results. Parameter b'^B was then identified from shear results for which $\cos\left(3\theta_\varepsilon^B\right) = 0$ and $\xi^B = 0$. Parameter a'^B was then deduced from uniaxial tensile conditions (i.e. either uniaxial tension or DENT) for which $\cos\left(3\theta_\varepsilon^B\right) = 1$ and ξ^B = 1314 MPa. Here again, four tests were used to identify the fracture criterion. The results are also reported in Table 5.

The ratios between minor and major axes of the elliptic section of the two fracture criteria are close to each other (1.23 for Eq. (15) and 1.20 for Eq. (16)). Predictions of notch opening at fracture are non-conservative with the model of Eq. 15. The model of Eq. (16) yields conservative predictions of displacement at fracture for all tests except for ungrooved DENS specimen, for which the loading path is far from being radial in the gauge region. For all other specimens, fracture is predicted to initiate at the same integration point (i.e., same location in the specimen) by the two models. The difference between "experimental" values and model predictions, Δ, was quantified as follows:

$$\Delta = \sum_i \sqrt{\frac{\left(\sigma_i^{\exp} - \sigma_i^{crit}\right)^2}{\left(\sigma_i^{crit}\right)^2}} \quad (17)$$

In Eq. (17), for any test *i* and for any fracture initiation criterion *crit*, (namely, critical value of σ_B, critical value of τ_{max}, Eq. (15) or Eq. (16)), $\sigma_i^{\exp}$ and σ_i^{crit} are respectively the "experimental" value of (Barlat) equivalent stress at fracture and the corresponding model prediction using criterion *crit*.

Introducing the hydrostatic pressure into the fracture initiation criterion divides the value of Δ by two (Table 5). Predictions are mainly improved in the left part of the RD-FLD, at the expense of biaxial stretching. Further work is necessary to also improve prediction in the right part of the RD-FLD. This point is not critical, however, for this material and targeted automotive application, in usual forming conditions. The model could further be improved by using a more sophisticated function of hydrostatic pressure. This is, however, beyond the scope of this study due to the low number of "experimental" results involving similar values of Lode angle and significantly different values of hydrostatic pressure. The model of Eq. 16 was thus considered to satisfactorily represent the RD-FLD for the considered material. Note that many tests (17) were used to identify the constitutive parameters (but a lower number could have been used, in particular in reverse shear). On the other hand, only four tests were used to identify the fracture criterion, some of them being the same as those used for identification of constitutive parameters.

Table 5: Fracture initiation criteria parameters for loading along RD and accuracy of model predictions.

Fracture criterion	Critical values of stress:		Function of σ_B and Lode angle (Eq. 15)		Function of hydrostatic pressure, σ_B and Lode angle (Eq. 16)			
Parameters	σ_B (MPa)	τ_{max} (MPa)	a^B (MPa)	b^B (MPa)	a'^B	b'^B	h^B	ξ_0 (MPa)
Adjusted values	2276	1050	2200	1850	1.12	0.93	0.13	15515
Δ calculated using tests involving minor strain *negative* or *positive* minor strains at fracture initiation locus)	0.55	0.54	0.41		0.27			
Δ calculated using tests involving *negative* minor strains at fracture initiation locus only	0.36	0.35	0.24		0.19			

5. Conclusions

An extensive experimental database has been built for the mechanical behaviour of a 22Mn-0.6C-0.2V TWIP steel. Several fracture criteria were identified on this basis. Main conclusions are as follows:

1. Anisotropic yield is satisfactorily represented with an anisotropic (Barlat-type) yield criterion for a variety of in-plane loading modes.
2. Taking the strong contribution of kinematic hardening into account is mandatory in the case of significantly non-radial loading path, but not useful in the case of monotonic tensile loading of smooth and notched specimens, for which a simple non-linear isotropic hardening equation provides very good estimates of macroscopic response and local strain fields.
3. Fracture occurs suddenly by nucleation and early coalescence of submicrometer-sized voids, although some damage develops as scarce, coarser voids well before fracture. Vanadium carbides as well as the occurrence of mechanical twinning are probably key parameters governing void nucleation.
4. The forming limit diagram was estimated using several fracture criteria together with the same formalism at that of the constitutive model. A simple function of hydrostatic stress, anisotropic equivalent stress and Lode angle (with a strain rate-based definition) satisfactorily represent fracture initiation conditions.
5. Such criterion relies on a particular loading direction (here, RD) and further work is required to develop a fracture initiation criterion based on the same formalism but more directly usable for the prediction of forming ability in more complex conditions such as deep drawing.

6. Acknowledgements

Technical help from A. Meddour, Y. Auriac (MINES ParisTech) and G. Petitgand, S. Douchamps and B. Remy (ArcelorMittal) is gratefully acknowledged. Introduction of kinematical hardening parameters varying with cumulative plastic strain was suggested by J.L. Chaboche (MINES ParisTech).

7. References

[Cornette et al, 2005] D. Cornette, P. Cugy, A. Hildenbrand, M. Bouzekri, G. Lovato, Ultra high strength FeMn TWIP steels for automotive safety parts. Rev. Métall. 12 (2005) 905–918, http://dx.doi.org/10.1051/metal:2005151

[Bouaziz et al, 2011] O. Bouaziz, S. Allain, C.P. Scott, P. Cugy, D. Barbier, High manganese austenitic twinning induced plasticity steels: A review of the microstructure properties relationships. Current Opinion in Solid State and Materials Science 15 (2011) 141–168, http://dx.doi.org/10.1016/j.cossms.2011.04.002

[Lee et al, 2011] S.-J. Lee, J. Kim, S. N. Kane, B.C. De Cooman, On the origin of dynamic strain aging in twinning-induced plasticity steels. Acta Mater. 59 (2011) 6809–6819, http://dx.doi.org/10.1016/j.actamat.2011.07.040

[Bayraktar et al, 2004] E. Bayraktar, F.A. Khalid, C. Levaillant, Deformation and fracture behaviour of high manganese austenitic steel. J. Mater. Process. Technol. 147 (2004) 145–154, http://dx.doi.org/10.1016/j.jmatprotec.2003.10.007

[Scavino et al, 2010] G. Scavino, F. D'Aiuto, P. Matteis, P. Russo Spena, D. Firrao, Plastic Localization Phenomena in a Mn-Alloyed Austenitic Steel. Metall. Mater. Trans. A, 41A (2010) 1493–1501, http://dx.doi.org/10.1007/s11661-010-0191-9

[Rémy, 1978] Rémy L. Kinetics of f.c.c. deformation twinning and its relationship to stress-strain behaviour. Acta Metall. 26 (1978) 443-451, http://dx.doi.org/10.1016/0001-6160(78)90170-0

[Idrissi et al, 2010] H. Idrissi, K. Renard, D. Schryvers, P.J. Jacques, On the relationship between the twin internal structure and the work-hardening rate of TWIP steels. Scr. Mater. 63 (2010) 961–964, http://dx.doi.org/10.1016/j.scriptamat.2010.07.016

[Gutierrez-Urrutia et al, 2010] I. Gutierrez-Urrutia, S. Zaefferer, D. Raabe, The effect of grain size and grain orientation on deformation twinning in a Fe-22wt.% Mn-0.6wt.% C TWIP steel . Mater. Sci. Eng. A527 (2010) 3552–3560, http://dx.doi.org/10.1016/j.msea.2010.02.041

[Barbier et al, 2009] D. Barbier, N. Gey, S. Allain, N. Bozzolo, M. Humbert, Analysis of the tensile behaviour of a TWIP steel based on the texture and microstructure evolutions. Mater. Sci. Eng. A500 (2009) 196–206, http://dx.doi.org/10.1016/j.msea.2008.09.031

[Chung et al, 2011] K. Chung, K. Ahn, D.-H. Yoo, K.H. Chung, M.-H. Seo, S.-H. Park, Formability of TWIP (twinning induced plasticity) automotive sheets. Int. J. Plast. 27 (2011) 52–81, http://dx.doi.org/10.1016/j.ijplas.2010.03.006

[Xu et al, 2012] L. Xu, F. Barlat, M.-G. Lee, Hole expansion of twinning-induced plasticity steel. Scr. Mater. 66 (2012) 1012-1017, http://dx.doi.org/10.1016/j.scriptamat.2012.01.062

[Dorn and Thomsen, 1947] J.E. Dorn, E.G. Thomsen, The ductility of metals under general conditions of stress and strain. Trans. Am. Soc. Met. 39 (1947) 741-772

[Swift, 1952] H.W. Swift, Plastic instability under plane stress, J. Mech. Phys. Solids 1 (1952) 1-18, http://dx.doi.org/10.1016/0022-5096(52)90002-1

[Hill, 1952] R. Hill, On discontinuous plastic states with special reference to localized necking in thin sheets, J. Mech. Phys. Solids 1 (1952) 19-30, http://dx.doi.org/10.1016/0022-5096(52)90003-3

[Marciniak and Kuczyński, 1967] Z. Marciniak, K. Kuczynski, Limits strains in the processes of stretch-forming sheet metal. Int. J. Mech. Sci. 9 (1967) 609-612, http://dx.doi.org/10.1016/0020-7403(67)90066-5

[De Cooman et al, 2008] B.C. De Cooman, L. Chen, H.S. Kim, Y. Estrin, S.K. Kim, H. Voswinckel, Review of the mechanical properties of high strength, high-Mn TWIP steels for automotive appications. International Conference on New Developments on Metallurgy and Applications of High

Strength Steels, 26-28 May, 2008, Buenos Aires, Argentina, Wiley, Paper #7, ISBN - 13: 9780873397292

[Wang et al, 2011] H. Wang, C. Berdin, M. Mazière, S. Forest, C. Prioul, A. Parrot, P. Le-Delliou, Portevin-Le Chatelier (PLC) instabilities and slant fracture in C-Mn steel round tensile specimens. Scripta Mater 64 (2011) 430-433, http://dx.doi.org/10.1016/j.scriptamat.2010.11.005

[Allain et al, 2008] S. Allain, P. Cugy, C. Scott, J.P. Chateau, A. Rusinek, A. Deschamps, The influence of plastic instabilities on the mechanical properties of a high-manganese austenitic FeMnC steel. Int. J. Mater. Res. 99 (2008) 734–738, http://dx.doi.org/10.3139/146.101693

[Lorthios et al, 2010] J. Lorthios, F. Nguyen, A.-F. Gourgues, T.F. Morgeneyer, P. Cugy, Damage observation in a high-manganese austenitic TWIP steel by synchrotron radiation computed tomography. Scr. Mater. 63 (2010) 1220–1223, http://dx.doi.org/10.1016/j.scriptamat.2010.08.042

[Abbasi et al, 2009] M. Abbasi, S. Kheirandish, Y. Kharrazi, J. Hejazi, The fracture and plastic deformation of aluminum alloyed Hadfield steels. Mater. Sci. Eng. A513-514 (2009) 72–76, http://dx.doi.org/10.1016/j.msea.2009.02.023

[Chung et al, 2011b] K. Chung, N. Ma, T. Park, D. Kim, D. Yoo, C. Kim, A modified damage model for advanced high strength steel sheets, Int. J. Plast. 27 (2011) 1485–1511, http://dx.doi.org/10.1016/j.ijplas.2011.01.007

[Beese et al, 2010] A.M. Beese, M. Luo, Y. Li, Y. Bai, T. Wierzbicki, Partially coupled anisotropic fracture model for aluminum sheets. Eng. Fract. Mech. 77 (2010) 1128–1152, http://dx.doi.org/10.1016/j.engfracmech.2010.02.024

[Scott et al, 2005] C. Scott, N. Guelton, S. Allain, M. Faral, The Development of a New Fe-Mn-C Austenitic Steel for Automotive Applications. Proc MS&T 2005 Conf. USA: Pittsburgh; 2005, ed. J.R. Fekete and R. Pradhan, (2005), ASM International, p. 1012-1023

[Allain et al, 2004] S. Allain, J.P. Chateau, O. Bouaziz, S. Migot, N. Guelton, Correlations between the calculated stacking fault energy and the plasticity mechanisms in Fe–Mn–C alloys. Mater. Sci. Eng. A387–389 (2004)158–162, http://dx.doi.org/10.1016/j.msea.2004.01.059

[Schumann 1972] V.H. Schumann, Martensitische Umwandlungen in austenitischen Mangan-Kohlenstoff-Stählen. Neue Hütte 17 (1972) S.605–609

[Yen et al, 2012] H.-W. Yen, M. Huang, C.P. Scott, J.-R. Yang, Interactions between deformation-induced defects and carbides in a vanadium-containing TWIP steel. Scr. Mater. 66 (2012) 1018-1023, http://dx.doi.org/10.1016/j.scriptamat.2012.02.002

[Scott et al, 2011] C. Scott, B. Remy, J.L. Collet, A. Cael, C. Bao, F. Danoix, B. Malard, C. Curfs, Precipitation strengthening in high manganese austenitic TWIP steels. Int. J. Mater. Res. 102 (2011) 538–549, http://dx.doi.org/10.3139/146.110508

[Malard et al, 2012] B. Malard, B. Remy, C. Scott, A. Deschamps, J. Chêne, T. Dieudonné, M.H. Mathon, Hydrogen trapping by VC precipitates and structural defects in a high strength Fe–Mn–C steel studied by small-angle neutron scattering, Mater. Sci. Eng. A536 (2012) 110–116, http://dx.doi.org/10.1016/j.msea.2011.12.080

[Dastur et al, 1981] Y.N. Dastur, W.C. Leslie, Mechanism of Work Hardening in Hadfield Manganese Steel. Metall. Trans. A, 12A (1981) 749-759, http://dx.doi.org/ 10.1007/BF02648339

[Owen and Grujicic, 1998] W.S. Owen, M. Grujicic, Strain aging of austenitic Hadfield manganese steel. Acta Mater. 47 (1998) 111-126, http://dx.doi.org/10.1016/S1359-6454(98)00347-4

[Canadinc et al, 2008] D. Canadinc, C. Efstathiou, H. Sehitoglu, On the negative strain rate sensitivity of Hadfield steel. Scr. Mater. 59 (2008)1103-1106, http://dx.doi.org/10.1016/j.scriptamat.2008.07.027

[Renard et al, 2010] K. Renard, S. Ryelandt, P.J. Jacques, Characterisation of the Portevin-Le Châtelier effect affecting an austenitic TWIP steel based on digital image correlation, Mater. Sci. Eng. A527 (2010) 2969-2977, http://dx.doi.org/10.1016/j.msea.2010.01.037

[Allain, 2004] Allain S. Multiscale thermomechanical characterisation and modelling of deformation and work-hardening mechanisms of high manganese austenitic steels, PhD thesis. Institut National Polytechnique de Lorraine; 2004 (in French).

[Chen et al, 2007] L. Chen, S. Birosca, H.S. Kim, S.K. Kim, B.C. De Cooman, Some aspects of thermo-mechanical properties of high Mn TWIP steels investigated by in-situ infrared thermography. Proc. AIST Steel Properties and Applications Conference Proceedings, Detroit, MI, 16-20 September, 2007, AIST, Warrendale, PA, 2007, Vol. 1, 173-183 (ISBN:978-160560133-5)

[Lebedkina et al, 2009] T.A. Lebedkina, M.A. Lebyodkin, J.P. Chateau, A. Jacques, S. Allain, On the mechanism of unstable plastic flow in an austenitic FeMnC TWIP steel. Mater. Sci. Eng. A519 (2009) 147-154, http://dx.doi.org/10.1016/j.msea.2009.04.067

[Zavattieri et al, 2009] P.D. Zavattieri, V. Savic, L.G. Hector, Jr, J.R. Fekete, W. Tong, Y. Xuan, Spatio-temporal characteristics of the Portevin-Le Châtelier effect in austenitic steel with twinning induced plasticity. Int. J. Plast. 25 (2009) 2298-2330, http://dx.doi.org/10.1016/j.ijplas.2009.02.008

[GOM] Aramis® Software, Optical 3D Deformation Analysis, Gesellschaft für Optische Messtechnik mbH, Braunschweig, Germany, http://www.gom.com/metrology-systems/system-overview/aramis.html (as on 15. April, 2015)

[Brünig et al, 2008] M. Brünig, O. Chyra, D. Albrecht, L. Driemeier, M. Alves, A ductile damage criterion at various stress triaxialities. Int. J. Plast. 24 (2008) 1731-1755, http://dx.doi.org/10.1016/j.ijplas.2007.12.001

[McClintock & Argon, 1966] F.A. McClintock and A.S. Argon, Mechanical Behavior of Materials, Addison-Wesley, Reading, MA (1966) 320-322.

[ASTM 1996] ASTM, B 871-96 standard test method for tear testing of aluminum alloy products, vol. 02-02, ASTM, 1996, pp. 1–7, http://dx.doi.org/10.1520/B0871-96

[Bouaziz et al, 2010] O. Bouaziz, S. Allain, Y. Estrin, Effect of pre-strain at elevated temperature on strain hardening of twinning-induced plasticity steels. Scr. Mater. 62 (2010) 713–715, http://dx.doi.org/10.1016/j.scriptamat.2010.01.040

[Bouaziz et al, 2008] O. Bouaziz, S. Allain, C. Scott, Effect of grain and twin boundaries on the hardening mechanisms of twinning-induced plasticity steels. Scr. Mater. 58 (2008) 484–487, http://dx.doi.org/10.1016/j.scriptamat.2007.10.050

[Dumay, 2008] A. Dumay, Improving physical and mechanical properties of FeMnXC TWIP steels - Influence of solid solution, precipitation hardening and composite effect. PhD thesis, Institut National Polytechnique de Lorraine, 2008 (in French)

[Besson and Foerch, 1997] J. Besson, R. Foerch, Large scale object-oriented finite element code design. Comput. Methods Appl. Mech. Engng 142 (1997) 165–187, p://dx.doi.org/10.1016/S0045-7825(96)01124-3

[Allain et al, 2004] S. Allain S, J.P. Chateau, D. Dahmoun, O. Bouaziz, Modeling of mechanical twinning in a high manganese content austenitic steel. Mater. Sci. Eng. A387–389 (2004) 272–276, http://dx.doi.org/10.1016/j.msea.2004.05.038

[Gil Sevillano, 2009] J. Gil Sevillano, An alternative model for the strain hardening of FCC alloys that twin, validated for twinning-induced plasticity steel. Scr. Mater. 60 (2009) 336–339, http://dx.doi.org/10.1016/j.scriptamat.2008.10.035

[Soulami et al, 2011] A. Soulami, K.S. Choi, Y.F. Shen, W.N. Liu, X. Sun, M.A. Khaleel, On deformation twinning in a 17.5% Mn–TWIP steel: A physically based phenomenological model. Mater. Sci. Eng. A528 (2011) 1402–1408, http://dx.doi.org/10.1016/j.msea.2010.10.031

[Favier and Barbier, 2012] V. Favier, D. Barbier, Micromechanical modelling of twinning-induced plasticity steels. Scr. Mater. 66 (2012), 972-977, http://dx.doi.org/10.1016/j.scriptamat.2011.12.017

[Steinmetz et al, 2013] D.R. Steinmetz, T. Jäpel, B. Wietbrock, P. Eisenlohr, I. Gutierrez-Urrutia, A. Saeed–Akbari, T. Hickel, F. Roters, D. Raabe, Revealing the strain-hardening behavior of twinning-induced plasticity steels: Theory, simulations, experiments. Acta Mater. 61 (2013) 494–510, http://dx.doi.org/10.1016/j.actamat.2012.09.064

[Liu et al, 2015] F. Liu, W.J. Dan, W.G. Zhang, Strain hardening model of twinning induced plasticity steel at different temperatures. Mater. Des. 65 (2015) 737-742, http://dx.doi.org/10.1016/j.matdes.2014.10.008

[Barlat et al, 1991] F. Barlat, D.J. Lege, J.C. Brem, A six-component yield function for anisotropic materials. Int. J. Plast. 7 (1991) 693-712, http://dx.doi.org/10.1016/0749-6419(91)90052-Z

[Bron and Besson, 2004] F. Bron, J. Besson, A yield function for anisotropic materials: application to aluminium alloys. Int. J. Plast. 20 (2004) 937-963, http://dx.doi.org/10.1016/j.ijplas.2003.06.001

[Laurent et al, 2009] H. Laurent, R.Grèze, P.Y. Manach, S. Thuillier, Influence of constitutive model in springback prediction using the split-ring test, Int. J. Mech. Sci. 51 (2009) 533-545, http://dx.doi.org/10.1016/j.ijmecsci.2008.12.010

[Shinohara et al, 2010] Y. Shinohara, Y. Madi, J. Besson, A combined phenomenological model for the representation of anisotropic hardening behavior in high strength steel line pipes, Eur. J. Mech. A/Solids, 29 (2010) 917-927, http://dx.doi.org/ 10.1016/j.euromechsol.2010.06.003

[Vladimirov et al, 2010] I.N.Vladimirov, M.P. Pietryga, S. Reese, Anisotropic finite elastoplasticity with nonlinear kinematic and isotropic hardening and application to sheet metal forming, Int. J. Plast. 26 (2010) 659-687, http://dx.doi.org/10.1016/j.ijplas.2009.09.008

[Besson et al., 2009] J. Besson, G. Cailletaud, J.-L. Chaboche, S. Forest, Non Linear Mechanics of Materials. Springer, 2009, ISBN-13: 978-9048133550

[Hosford, 1979] W. F. Hosford, On yield loci of anisotropic cubic metals, Proc. 7th North Am. Metalworking Conf., Society of Manufacturing Engineers, Dearborn, Michigan, 191–196 (1979). *Sorry, we did not find a doi number for this reference*

[Hosford, 1985] W.F. Hosford, Comments on anisotropic yield criteria, Int. J. Mech. Sci. 27 (1985) 423–427, http://dx.doi.org/10.1016/0020-7403(85)90032-3

[Logan and Hosford, 1980] R.W. Logan, W.F. Hosford, Upper-bound anisotropic yield locus calculations assuming <111>-pencil glide, Int. J. Mech. Sci. 22 (1980) 419–430, http://dx.doi.org/10.1016/0020-7403(80)90011-9

[Busch et al, 2014] C. Busch, A. Hatscher, M. Otto, S. Huinink, M. Vucetic, C. Bonk, A. Bouguecha, B.-A. Behrens, Properties and application of high-manganese TWIP-steels in sheet metal forming, Procedia Eng. 81 (2014) 939–944, http://dx.doi.org/10.1016/j.proeng.2014.10.121

[Lorthios, 2011] J. Lorthios, Damage of TWIP steels for automotive applications, PhD thesis, Ecole des Mines de Paris, France (in French), http://pastel.archives-ouvertes.fr/pastel-00689791 (as on 15. April, 2015)

[Dell and Gese, 2007] H. Dell, H. Gese, Private technical report; 13 July 2007.

[Hooputra et al, 2004] H. Hooputra, H. Gese, H. Dell, H. Werner, A comprehensive failure model for crashworthiness simulation of aluminium extrusions. Int. J. Crashworthiness 9 (2004) 449–463, http://dx.doi.org/10.1533/ijcr.2004.0289

[Dell et al, 2008] H. Dell, H. Gese, G. Oberhofer. In: Users' manual: MF GenYld + CrachFEM: theory, version 3.8, MATFEM Partnerschaft Dr Gese & Oberhofer, editor M. Oehm, 20 May 2008.

[Wierzbicki et al, 2005] T. Wierzbicki, Y. Bao, Y.-W. Lee, Y. Bai, Calibration and evaluation of seven fracture models. Int. J. Mech. Sci. 47 (2005) 719-743, http://dx.doi.org/10.1016/j.ijmecsci.2005.03.003

[Zadpoor et al, 2009] A.A. Zadpoor, J. Sinke, R. Benedictus, Formability prediction of high strength aluminum sheets. Int. J. Plast. 25 (2009) 2269–2297 , http://dx.doi.org/10.1016/j.ijplas.2009.02.005

[McClintock, 1968] F.A. McClintock, A criterion for ductile fracture by the growth of holes. J. Appl. Mech. 35 (1968) 363-371, http://dx.doi.org/10.1115/1.3601204

[Rice and Tracey, 1969] J. Rice, D.M. Tracey, On the ductile enlargement of voids in triaxial stress fields. J. Mech. Phys. Sol. 17 (1969) 201-217, http://dx.doi.org/10.1016/0022-5096(69)90033-7

[Oyane et al, 1980] M. Oyane, T. Sato, K. Okimoto, S. Shima, Criteria for Ductile Fracture and Their Applications. J. Mech. Work. Technol., 4 (1980) 65–81, http://dx.doi.org/10.1016/0378-3804(80)90006-6

[Fricker and Meckbach, 1999] R. Jeltsch-Fricker, S. Meckbach, Parabolische Mohrsch Bruchbedingung in Invariantendarstellung für spröde isotrope Werkstoffe, Z. Angew. Math. Mech. 79 (1999) 465-471, http://dx.doi.org/10.1002/(SICI)1521-4001(199907)79:7<465::AID-ZAMM465>3.0.CO;2-3

[Xue and Wierzbicki, 2008] L. Xue, T. Wierzbicki, Ductile fracture initiation and propagation modeling using damage plasticity theory, Eng. Fract. Mech. 75 (2008) 3276–3293, http://dx.doi.org/10.1016/j.engfracmech.2007.08.012

[Bai and Wierzbicki, 2010] Y. Bai, T. Wierzbicki, Application of extended Mohr-Coulomb criterion to ductile fracture, Int. J. Fract. 161 (2010) 1-20, http://dx.doi.org/10.1007/s10704-009-9422-8

[Rudnicki and Rice, 1975] J.W. Rudnicki, J.R. Rice, Conditions for the localization of deformation in pressure-sensitive dilatant materials, J. Mech. Phys. Sol. 23 (1975) 371-394, http://dx.doi.org/10.1016/0022-5096(75)90001-0

[Needleman and Rice, 1978] A. Needleman, J.R. Rice, Limits to ductility set by plastic flow localization. In: Mechanics of Sheet Metal Forming, (ed. by D. P. Koistinen and N.-M. Wang), Plenum Press, New York, 237–265 (1978), http://dx.doi.org/10.1007/978-1-4613-2880-3